# Implementation of rotational resistance models: a critical appraisal

# Implementation of rotational resistance models: a critical appraisal

Xin Huang*[a,b], Kevin J. Hanley[c], Catherine O'Sullivan[d], Chung-Yee Kwok[e]

[a] *Department of Geotechnical Engineering, Tongji University, 1239 Siping Road, Shanghai 200092, China*

[b] *Key Laboratory of Geotechnical and Underground Engineering of Ministry of Education, Tongji University, 1239 Siping Road, Shanghai 200092, China*

[c] *Institute for Infrastructure and Environment, School of Engineering, The University of Edinburgh, Edinburgh EH9 3JL, United Kingdom*

[d] *Skempton Building, Department of Civil and Environmental Engineering, Imperial College London, London SW7 2AZ, United Kingdom*

[e] *Haking Wong Building, Department of Civil and Environmental Engineering, The University of Hong Kong, Pokfulam Road, Hong Kong*

** Corresponding author: Email: xhuang@tongji.edu.cn Phone: +86-21-65984551*

## Abstract

Contact models that simulate rotational resistance at the particle contacts have been proposed as a means to capture the shape effect in DEM simulations. This contribution critically explores some of the key issues relating to implementation of rotational resistance models; these include the need for physically meaningful model parameters, the impact of the model on the overall numerical stability / critical time increment for the DEM model, model validation and assessment of model performance relative to real physical materials. The discussion is centred around a rotational resistance model that captures the resistance provided by interlocking asperities on the particle surface. An expression for the maximum permissible integration timestep to ensure numerical stability is derived for DEM simulations when rotational resistance is incorporated. Analytical solutions for some single-contact scenarios are derived for model validation. The ability of this type of model to provide additional fundamental insight into granular material behaviour is demonstrated by using particle-scale analysis of triaxial compression simulations to examine the roles that contact rolling and sliding have on the stability of strong force chains.

## Keywords

Granular Media; Particle Shape; Discrete Element Method; Rolling; Twisting; Rotational Resistance

## 1. Introduction

Soil grains have distinct shape characteristics, e.g., sphericity, roundness and roughness, that depend upon their production, transportation and deposition histories as well as their mineralogical composition. Different degrees of shape irregularity result in different degrees of interlocking between soil grains. The significance of particle shape on soil behaviour has been reported in many experimental studies (e.g., Cho et al. 2006; Shin & Santamarina, 2013; Yang & Wei, 2012). Recent research of Payan et al. (2016a,b) showed that particle shape has a pronounced influence on the small-strain stiffness and damping ratio of sand.

Even if very high coefficients of friction are used, the peak and critical-state angles of shearing resistance observed in DEM simulations using spherical particles are significantly below what is expected for a real sand (Huang et al., 2014; Yang et al., 2012; Thornton, 2000). These differences arise due to the differences in geometry between spheres and real sand grains. One approach to capture the non-spherical nature of soil grains in DEM simulations is to introduce rotational resistance at the contacts between discs or spheres to simulate the interlocking effect between irregular particles; this approach is conceptually simple and less computationally expensive than directly simulating non-spherical particles either using irregular particles or by clustering small particles. Since the pioneering work of Iwashita & Oda (1998), a number of rotational resistance models have been proposed and applied in DEM simulations including the 2D models proposed by Tordesillas and Walsh (2002), Jiang et al. (2005), and Mohamed and Gutierrez (2010); and the 3D models proposed by Jiang et al. (2015), Zhao and Guo (2014), Plassiard et al. (2009) and Zhou et al. (1999). Use of these models has been shown to increase the strength and dilatancy of DEM assemblies. Thus, the use of rotational resistance brings the DEM simulation results using spherical particles closer to the real behaviour of soils. Using spherical or circular particles, rotational resistance can alternatively be achieved by bonding particles together so that a single particle comprises multiple degrees of freedom (e.g. Jensen, et al., 1999), clumping particles so that each particle is one degree of freedom and the constituent particles are used only for contact detection (e.g. Thomas and Bray, 1999), or inhibiting particle rotation completely e.g. Calvetti (2008). These approaches have differing computational cost implications. Inhibiting rotations will not increase the computational cost of simulations, however this is an extreme model and we know some rotation takes place in real materials (e.g. Oda and Kazama, 1998). Accurately capturing the geometry of realistic grain shapes requires hundreds of sub-particles to be used to get something approaching a realistic topology (Garcia et al. 2009) and even then only the form of the particle shape is captured, while the surface topology differs from real particles. Consequently even where a clumping / cluster model approach is used a contact model that enables control of rotational resistance is advantageous to improve model fidelity.

This study explores some of the critical issues related to implementation of rotational resistance models that have been neglected in most of the prior studies in the literature. Firstly, a model that accounts for the extent of interlocking at the contacts as well as the asperity strength is briefly introduced. Focussing on this model, some crucial general implementation issues are then discussed. A general procedure to identify a numerically stable critical timestep when rotational resistance is considered is detailed. Closed-form solutions pertinent to several representative particle-and-wall contacting scenarios are derived which serve to both analyze model accuracy and check implementation in a DEM code. Finally, the model's relevance to physical materials is demonstrated in simulations of triaxial compression; how rotational resistance influences force-chain stability and hence the overall behaviour are explored.

## 2. Model Description

### 2.1 Physical origins of rotational resistance

Both particle form (overall shape) and the surface texture (presence of asperities) contribute to rotational resistance via differing mechanisms (Johnson, 1985):

*a) Deviation of the branch vector direction from the contact normal direction*

For non-spherical particles, the branch vector direction ($\overrightarrow{O_A O_B}$) is no longer coincident with the contact normal direction $\vec{f}_n$ (Figure 1 (a)). Under such circumstances, the contact normal does not pass through the particle centroid and can impose a moment on the particle or generate a resistance to a moment applied elsewhere. This mechanism is closely related to the particle sphericity.

*b) Interlocking effects*

The non-convex, rough nature of particle surfaces contributes an interlocking effect which can be illustrated by considering the relative motion between the two gears shown in Figure 1 (b). When these two gears roll over each other, the contact force (*f*) at the 'teeth' induces a moment that opposes the relative rolling direction for both particles in contact. Differentiating features that define particle shape and features that define roughness is subjective; the type of micro-asperities sized $\leq$ 1μm considered by Senetekis et al. 2013 and Otsubo et al. 2015 will not measurably contribute to rotational resistance. Cavarretta et al. (2010) proposed a lower limit of 0.1 for measurements of roundness and so the 'teeth' considered herein can be taken as features including corners used to define roundness and large asperities that are up to 0.05D where D is a representative particle diameter. The resistance to the relative angular motion depends on the penetration of the 'teeth' which is associated with the external force (*F*) acting in the normal direction. A larger *F* should lead to deeper penetration of the two particles which thereby increases the rotational resistance.

The first mechanism can only be captured when non-spherical particles are used, while the second mechanism can be approximated by employing rotational springs at the contacts using spherical particles. It is this second type of rotational resistance that is considered here.

### 2.2 Model Formulations

The rotational resistance model used herein is similar to the model proposed by Jiang et al. (2015). A complete description of the model is provided as supplementary information and can be accessed through the journal website, and a concise overview is given here. It is assumed that the interaction between two contacting particles occurs over a finite circular contact area. The contact is idealised to be composed of uniformly-distributed elastic springs in both the normal and tangential directions. The mean contact stiffnesses ($\bar{k}_n$ and $\bar{k}_s$) of the equivalent uniformly-distributed springs are equal to their equivalents for a single spring system ($k_n$ and $k_s$) divided by the modified area $A'$, i.e., $\bar{k}_n = k_n/A'$, $\bar{k}_s = k_s/A'$ and $A' = \pi(\delta B)^2$, in which $B$ is the radius of the contact plane and $\delta$ is a shape parameter accounting for the undulating / nonsmooth nature of the contact surface.

The rotational resistance is decomposed into a rolling component $M_r$ opposing the rotational motion around axes in the contact plane and a twisting component $M_t$ counteracting the rotational motion about the contact normal. $M_r$ and $M_t$ are calculated according to Eq. 1:

$$\begin{cases} M_{r,i} = \overline{k_n} I_i \theta_{r,i} \;\&\; M_{r,i} \le \kappa f_n R_r \;\; (i = x, y) \\ M_{t,i} = \overline{k_s} J_z \theta_{t,i} \;\&\; M_{t,i} \le \mu\kappa f_n R_r \;\; (i = z) \end{cases} \qquad \text{(Eq. 1)}$$

in which $I_i = \frac{\pi}{4}(\delta B)^4$ is the area moment of inertia of a circular area with respect to the $i^{\text{th}}$ axis in the contact plane, $J_z = \frac{\pi}{2}(\delta B)^4$ is the polar area moment of inertia with respect to the contact normal (z axis), $\kappa$ is a strength index which relates the compressive strength of asperities to the normal contact force, and $\theta_r^i$ and $\theta_t$ are the relative rolling and twisting angles, respectively. The reduction of angularity and associated reduction in rotational resistance due to asperity damage are not considered in Eq. 1. The derivation of Eq. 1 is based on a local coordinate system ($x$-$y$-$z$) with the $z$ axis coinciding with the contact normal; therefore, transformations between the local coordinate system ($x$-$y$-$z$) and the global coordinate frame (X-Y-Z) are necessary.

Eq. 1 is a reduced version of Jiang et al. (2015) and has a reasonable physical basis. When compared with traditional DEM only two additional model parameters have been introduced, $\delta$ and $\kappa$, both of which have clear physical meanings: $\delta$ is related to irregularity of particle geometry while $\kappa$ relates the compressive strength of the asperities to the normal force. In reality, the asperities for a certain contact area may differ in size as well as in strength, and thus damage of the asperities may occur progressively rather than instantaneously. Therefore, it is difficult to assign a specific value to $\kappa$. Here

$\kappa$ was restricted to be <1; $\kappa$=1 represents a global failure of the asperities at the contact area. The model can be classified as an elasto-plastic model which yields the most numerically stable and realistic results (Ai et al., 2011).

Determination of the relative rotation, $\theta_r^i$ , here has followed Bardet (1994) and Jiang et al. (2005). The model was implemented into a modified version of the LAMMPS code (Plimpton, 1995). The transformation between local and global coordinates was achieved through quaternion operations. More details about the derivation and implementation of Eq. 1 are provided in Huang (2014).

## 3 The critical timestep

Prior implementations of rolling resistance have not explicitly considered numerical stability. However, this is important because the stability of the central difference-type integration schemes used in most DEM codes is conditional, requiring the integration timestep to be smaller than a critical value $\Delta t_{crit}$. O'Sullivan and Bray (2014) showed that a smaller $\Delta t_{crit}$ is required when the rotational degrees of freedom are taken into account. Since both the rolling and twisting resistances affect the angular motion, it is necessary to examine whether $\Delta t_{crit}$ should be more or less restrictive in the presence of these resistances. The commonly-used explicit second-order velocity-Verlet integration scheme is considered here. For a linear, undamped system, $\Delta t_{crit}$ can be determined by Eq. 2 (Belytschko, 1983):

$$\Delta t_{crit} = \frac{2}{\omega_{max}} \qquad \text{(Eq. 2)}$$

in which $\omega_{max} = \sqrt{\lambda_{max}}$ is the maximum natural frequency of the discrete system and $\lambda_{max}$ is the maximum eigenvalue of the $[M^{-1}][K]$ matrix ($[M]$ is the mass matrix and $[K]$ is the stiffness matrix of the entire system). Considering that $\lambda_{max} \leq {\lambda^e}_{max}$ for individual elements, where ${\lambda^e}_{max}$ is the maximum eigenvalue of the $[M]^{e-1}[K]^e$ matrix ($\boldsymbol{e}$ denotes a single element and the same notation is used in the following discussion), Eq. 2 can be expressed as:

$$\Delta t_{crit} = \frac{2}{\sqrt{{\lambda^e}_{max}}} \qquad \text{(Eq. 3)}$$

Following the approach of O'Sullivan & Bray (2004) and PFC3D (Itasca Consulting Group, 2007), the particles and contacts of a discrete element system are considered to be analogous to the nodes and elements of a finite element mesh, respectively (Figure 2(a)). A local stiffness matrix, analogous to a single element stiffness matrix in the finite element method, can be created for each contact. As indicated by Eq. 3, assuming that the translational and rotational degrees of freedom are uncoupled, $\Delta t_{crit}$ can be selected as the smallest critical timestep of individual elements (contacts) considering all degrees of freedom.

Considering the simplest case comprising only two particles (Figure 2(b)), there are two frames of reference: the global coordinate system (X,Y,Z) and the local coordinate system (*x*,*y*,*z*) at the contact with the *z* axis being coincident with the contact normal direction. The force-displacement law gives,

$$[F]^e = \left[K\right]^e [\mathrm{d}]^e = [\mathrm{T}]^{eT} [\mathrm{K}_L]^e [\mathrm{T}]^e [\mathrm{d}]^e \quad \text{(Eq. 4)}$$

$[T]^{\mathrm{e}}$ is the global-to-local transformation matrix, and $[K]^e$ and $[\mathrm{K}_L]^e$ are the contact stiffness matrices in the global and local coordinate systems, respectively. $[\mathrm{K}_L]^e$ is diagonally symmetric. For spherical particles, it can be expressed as Eq. 5 in which $k_{\theta,n}$ is the twisting resistance stiffness and the global displacement vector $[d]^e$ is given in Eq. 6.

$$[\mathrm{K}]_L^e = \begin{bmatrix}
k_t & 0 & 0 & 0 & k_t r_A & 0 & -k_t & 0 & 0 & 0 & k_t r_B & 0 \\
0 & k_t & 0 & k_t r_A & 0 & 0 & 0 & -k_t & 0 & k_t r_B & 0 & 0 \\
0 & 0 & k_n & 0 & 0 & 0 & 0 & 0 & -k_n & 0 & 0 & 0 \\
0 & k_t r_A & 0 & k_t r_A^2 - k_r & 0 & 0 & 0 & -k_t r_A & 0 & k_t r_A r_B + k_r & 0 & 0 \\
k_t r_A & 0 & 0 & 0 & k_t r_A^2 - k_r & 0 & -k_t r_A & 0 & 0 & 0 & k_t r_A r_B + k_r & 0 \\
0 & 0 & 0 & 0 & 0 & -k_{\theta,n} & 0 & 0 & 0 & 0 & 0 & k_{\theta,n} \\
-k_t & 0 & 0 & 0 & -k_t r_A & 0 & k_t & 0 & 0 & 0 & -k_t r_B & 0 \\
0 & -k_t & 0 & -k_t r_A & 0 & 0 & 0 & k_t & 0 & -k_t r_B & 0 & 0 \\
0 & 0 & -k_n & 0 & 0 & 0 & 0 & 0 & k_n & 0 & 0 & 0 \\
0 & k_t r_B & 0 & k_t r_A r_B + k_r & 0 & 0 & 0 & -k_t r_B & 0 & k_t r_B^2 - k_r & 0 & 0 \\
k_t r_B & 0 & 0 & 0 & k_t r_A r_B + k_r & 0 & -k_t r_B & 0 & 0 & 0 & k_t r_B^2 - k_r & 0 \\
0 & 0 & 0 & 0 & 0 & k_{\theta,n} & 0 & 0 & 0 & 0 & 0 & -k_{\theta,n}
\end{bmatrix} \quad \text{(Eq. 5)}$$

$$[d]^e = \begin{bmatrix} u_A & v_A & w_A & \theta_{x,A} & \theta_{y,A} & \theta_{z,A} & u_B & v_B & w_B & \theta_{x,B} & \theta_{y,B} & \theta_{z,B} \end{bmatrix}^T \quad \text{(Eq. 6)}$$

Assuming the nodal (particle) mass is equally distributed to the elements (contacts) that it participates in, the mass matrix for the contact linking particle *A* and particle *B* illustrated in Figure 2(b) can be expressed by Eq. 7, in which $n_A^c$ and $n_B^c$ are the numbers of contacts involving particles A and B respectively.

Calculating the eigenvalues of $[M]^{e-1}[T]^{T}[K]_L^e[T]$ is equivalent to the calculation of the eigenvalues of $[M]^{e-1}[K]_L^e$ (e.g. Golub and Van Loan, 1983). The global mass matrix $[M]^{\mathrm{e}}$ is identical to the local mass matrix $[M]_L^e$ due to the axisymmetric nature of spherical particles. Thus, $\Delta t_{crit}$ can be determined using Eq. 5 and Eq. 7. Considering the extreme case, i.e., two smallest particles with identical mass of *m*, moment of inertia of *I* and the same number of neighbouring particles, $n_c$, (i.e., $m_A$=$m_B$= *m*, $I_A$=$I_B$=*I* and $n_A^c = n_B^c = n_c$) , and ignoring the zero and identical eigenvalues, $\lambda^e{}_{max} = max\left(\frac{2k_t \cdot m \cdot n_c . r^2 + 2I \cdot k_t \cdot n_c}{I \cdot m}, \frac{2k_n n_c}{m}, \frac{2k_r n_c}{I}, \frac{2k_{\theta,n}}{I}\right)$ . For spherical particles ($I$=2/5$mr^2$), $\lambda^e{}_{max} = max\left(\frac{7k_t n_c}{m}, \frac{2k_n n_c}{m}, \frac{2k_r n_c}{I}, \frac{2k_{\theta,n}}{I}\right)$. Thus $\Delta t_{crit}$ is not a constant but varies during the simulation as the

number of contacts varies. The contact width is far smaller than the particle radius, which gives $k_r = k_n \frac{(\delta B)^2}{4} << k_n {r_A}^2$ and $\left|k_{\theta,n}\right| = k_t \frac{(\delta B)^2}{2} << k_t {r_A}^2$ . Hence, $\frac{2k_r n_c}{I} \ll \frac{5k_n n_c}{m}$ and $\frac{2|k_{\theta,n}|}{I} \ll \frac{5k_t}{m}$. According to the Hertz-Mindlin theory, the stiffness ratio $\frac{2}{3} \leq \frac{k_t}{k_n} \leq 1$ (Thornton et al., 2013; Zhang and Makse, 2005), which gives $\frac{14k_n n_c}{3m} \leq \frac{7k_t n_c}{m} \leq \frac{7k_n n_c}{m}$. Therefore, it is usually safe to use ${\lambda^e}_{max} = \frac{7k_t n_c}{m}$, which is also the maximum eigenvalue of $[M]^{e-1}[K]^e_L$, when rotational resistance is absent to estimate the critical timestep from Eq. 3. Thus, inclusion of rotational resistance does not decrease the critical timestep for the range of the stiffness ratios that can reasonably be expected based on Hertz-Mindlin contact mechanics.

$$
[M]^e_L = \begin{bmatrix}
\frac{m_A}{n_A^c} & 0 & 0 & 0 & 0 & 0 & 0 & 0 & 0 & 0 & 0 & 0 \\
0 & \frac{m_A}{n_A^c} & 0 & 0 & 0 & 0 & 0 & 0 & 0 & 0 & 0 & 0 \\
0 & 0 & \frac{m_A}{n_A^c} & 0 & 0 & 0 & 0 & 0 & 0 & 0 & 0 & 0 \\
0 & 0 & 0 & \frac{{I^x}_A}{n_A^c} & 0 & 0 & 0 & 0 & 0 & 0 & 0 & 0 \\
0 & 0 & 0 & 0 & \frac{{I^y}_A}{n_A^c} & 0 & 0 & 0 & 0 & 0 & 0 & 0 \\
0 & 0 & 0 & 0 & 0 & \frac{{I^z}_A}{n_A^c} & 0 & 0 & 0 & 0 & 0 & 0 \\
0 & 0 & 0 & 0 & 0 & 0 & \frac{m_B}{n_B^c} & 0 & 0 & 0 & 0 & 0 \\
0 & 0 & 0 & 0 & 0 & 0 & 0 & \frac{m_B}{n_B^c} & 0 & 0 & 0 & 0 \\
0 & 0 & 0 & 0 & 0 & 0 & 0 & 0 & \frac{m_B}{n_B^c} & 0 & 0 & 0 \\
0 & 0 & 0 & 0 & 0 & 0 & 0 & 0 & 0 & \frac{{I^x}_B}{n_B^c} & 0 & 0 \\
0 & 0 & 0 & 0 & 0 & 0 & 0 & 0 & 0 & 0 & \frac{{I^y}_B}{n_B^c} & 0 \\
0 & 0 & 0 & 0 & 0 & 0 & 0 & 0 & 0 & 0 & 0 & \frac{{I^z}_B}{n_B^c}
\end{bmatrix} \quad \text{(Eq. 7)}
$$

## 4 Verification scenarios for model implementation

To verify the implementation of the developed model, some simple scenarios were created in which the particle motion could be predicted analytically.

*A single ball spinning on a frictionless flat plane*

The first case considered is the motion of a single ball on a frictionless plane ($\mu$=0) (Figure 3(a)). Gravity was applied to the ball along with a local damping ratio value of 0.5. DEM calculation cycles were performed until the ball came to rest, after which damping was disabled. Then an initial rotational velocity ($\omega_{x,0}$ = -10 rad/s) was applied around the *x*-axis which passes through the centroid of the ball and lies in the plane. The equation of angular motion for this case is:

$$I_x\ddot{\theta_x} = -k_r\theta_x \quad \text{(Eq. 8)}$$

Solving Eq. 8, the angular velocity $\omega_x$ follows a harmonic pattern of motion:

$$\omega_x = \omega_{x,0}\cos(\sqrt{k_r/I_x}t) \quad \text{(Eq. 9)}$$

in which $k_r$ is the rolling stiffness and $I_x$ is the moment of inertia about the *x* axis. If the limiting value $M_r^m (= \kappa f_n r$ in Eq. 1) set for the rolling resistance is higher than the accumulated rolling resistance at the point when the angular velocity approaches zero, i.e., $M_r^m \geq (M_r)_{\omega_x=0} = \omega_{x,0}\sqrt{Ik_r} \approx 6.99e-5\ Nm$, the ball will rotate around the *x* axis exactly following Eq. 9. In this case, the system response is elastic and there is no energy dissipation. This is verified in Figures 3(b)-(c) which shows that when there is no limit set for the rolling resistance, the angular motion obtained in the LAMMPS simulation matches that predicted by Eq. 9. The timestep used in this simulation is $1 \times 10^{-6}\ s$ which is slightly smaller than the calculated $\Delta t_{crit} = min\left(2\sqrt{\frac{m}{k_n}}, 2\sqrt{\frac{I}{k_r}}\right) \approx 7.5 \times 10^{-6}\ s$ according to Eq. 3 (note that since the surface is frictionless, the shear force and twisting components in Eq. 5 can be eliminated).

If the rolling resistance is restricted to take a value that is lower than $(M_r)_{\omega_x=0}$, the motion of the ball will be rather complex. In such a case, three stages of motion can be identified:

- Stage-I ($0<t\leq t_1$): the ball moves following the harmonic motion as defined by Eq. 9 until the accumulated rolling resistance reaches the limit value $M_r^m$
- Stage-II I ($t_1<t\leq t_2$): the torque acting on the ball is constant and thus the angular velocity approaches zero linearly with time
- Stage-III I ($t_2<t\leq t_3$): when the angular velocity approaches zero, driven by $M_r^m$ the ball starts to rotate in the direction opposite to $\omega_{x,0}$, i.e., back rolling takes place. Under such circumstances, the direction of the rolling resistance increment shifts and the ball's motion follows:

$$I_x\ddot{\theta}_x = -k_r(\theta_x - (\theta_x)_{\omega=0}) + M_r^m \quad \text{(Eq. 10)}$$

The angular velocity for the aforementioned three stages of motion can be expressed by Eq. 11:

$$\omega_x = \begin{cases} \omega_{x,0}\cos(\sqrt{I/\mathrm{k}_r}\,\mathrm{t}), \quad \mathrm{t} \le \mathrm{t}_1 \;\; \textit{StageI} \\ \dfrac{\omega_{x,0}}{|\omega_{x,0}|} M_r^m \cdot (t - t_1)/I + \omega_{x,0}\cos(\sqrt{I/\mathrm{k}_r}\,\mathrm{t}_1), \quad t_1 < \mathrm{t} \le t_2 \;\; \textit{StageII} \\ -\dfrac{\omega_{x,0}}{|\omega_{x,0}|} M_r^m \cdot \sqrt{I/\mathrm{k}_r} \cdot \sin(\sqrt{I/\mathrm{k}_r}(t - t_2))/I, \; \mathrm{t} > \mathrm{t}_2 \;\; \textit{StageIII} \end{cases} \quad \text{(Eq. 11)}$$

in which $t_1 = \sin^{-1}(M_r^m / \omega_{x,0} / \sqrt{Ik_r}) \cdot \sqrt{I/\mathrm{k}_r}$ marks the transition instant from Stage I to Stage II, $t_2 = t_1 + I\omega_{x,0}\cos(\sqrt{I/\mathrm{k}_r}\,\mathrm{t}_1)/M_r^m$ defines the transition point from Stage II to Stage III and $M_r^m = \kappa f_n r$ is the limiting value for the rolling resistance.

Energy dissipation only takes place during Stage II at which the plastic limit is reached; Stage I and Stage III are purely elastic. Eq. 11 reflects two distinct roles of $\kappa$ and $\delta$ for the current model: $\kappa$ defines $M_r^m$ and thus controls the energy dissipation rate (the slope of Stage II) while $\delta$ determines the frequency of the harmonic motion and thus quantifies the transformation rate between the kinetic energy and strain energy stored in the rolling springs. Figure 4 illustrates the three-stage motion defined by Eq. 11 for $\kappa$=0.5. The input parameters are the same as indicated in Figure 3(a). Again, the DEM simulation results are in good agreement with the theoretical values.

The twisting characteristics (spinning around the contact normal (*z* axis)) are similar to those described above and therefore are not discussed here.

*A single ball moving along a frictional flat plane*

To investigate the interaction between the frictional force and the rolling resistance moment, the scenario shown in Figure 5(a) is considered. Instead of giving an initial angular velocity, the ball is assigned an initial translational velocity of 0.01 m/s in the *x* direction after completing the settling process discussed above. The translational movement of the ball generates a shear force that is opposite to the motion direction. This shear force induces angular motion around the *y* axis. The input parameters are identical to the previous case, except the friction coefficient was set at 0.25. The initial translational velocity and friction coefficient were chosen so that the sliding limit was reached in the first integration timestep, allowing the motion of the ball to be determined analytically. Figures 5(b) and 5(c) respectively show the evolution of the translational and angular velocity with time. For both motions, two distinct stages can be identified:

- Stage I: The shear force ($f_s$) is constant and equal to the limiting value $\mu f_n$. Therefore the translational velocity ($V_x$) decreases linearly with time, while the angular velocity initially follows the harmonic pattern defined by Eq. 12. As shown in Figure 5(c), the measured angular motion at Stage I coincides with the predicted motion defined by Eq. 12.

$$\omega_y = \frac{f_s R}{k_r}\sqrt{\frac{k_r}{I}}\sin\left(\sqrt{\frac{k_r}{I}}t\right) \quad \text{(Eq. 12)}$$

- Stage II: After $V_x$ reaches zero, $f_s$ starts to decrease and the equation of the angular motion becomes:

$$I\ddot{\theta} = (\mu f_n - k_t(\theta - \theta_{t1})r + k_t s(\theta)) - k_r(\theta - \theta_{t1}) \quad \text{(Eq. 13)}$$

in which $s(\theta)$ is the relative displacement at the contact due to the translational movement. Since no closed-form solution can be found for Eq. 13, no direct comparison can be made between the simulation data and the theoretical values.

The equations and the procedures described above are applicable to preliminarily validate the implementation of rotational resistance models before performing large simulations.

## 5. DEM simulations incorporating rotational resistance

### 5.1 Simulation overview

A numerical cloud composed of 20,164 non-contacting particles with a particle size distribution (PSD) approximating that of Toyoura sand as shown in Figure 6 was created within a cubic periodic cell. The cloud was then isotropically compressed to specified stress levels. Different inter-particle friction coefficients and rotational model parameters were used during this stage to generate samples with varying void ratios prior to shearing. A simplified Hertz-Mindlin contact model (Thornton et al., 2013; Zhang and Makse, 2005) was used. The particle shear modulus (G) and Poisson's ratio ($\nu$) were taken to be 29 GPa and 0.12 respectively. For the simplified Hertz-Mindlin model, the ratio of the equivalent stiffnesses $\frac{k_t}{k_n} = \frac{2(1-\nu)}{2-\nu} \approx 0.94$, and thus $\lambda^e{}_{max} = \frac{7k_t n_c}{m}$. An $n_c$ value of 4 was chosen (the minimum number of contacts required to maintain the mechanical stability of individual particles in a frictional system) as the smallest particles are unlikely to participate in force transmission. This leads to $\Delta t_{crit} = 0.378\sqrt{\frac{m}{k_t}}$. A reduced critical timestep of $0.1\sqrt{\frac{m}{k_t}} \approx 5.38e^{-9}s$ was used for all the simulations.

### 5.2 Stress-strain behaviour during shearing

Figure 7 shows the influence of $\kappa$ on the stress-deformation behaviour of a numerical assembly during triaxial shearing of samples that were initially isotropically compressed to a stress level of 100 kPa. So that the initial conditions were the same, the rotational resistance model was switched off in all the

samples during the compression phase and all samples had a void ratio of $e_0$=0.646 at the start of shearing. The samples were then subjected to drained triaxial shearing. $\mu$=0.25 and $\delta$ = 1 were used during both isotropic compression and triaxial shearing. Four $\kappa$ values were investigated and one additional simulation was performed without setting a limiting value for the rolling or twisting resistance. The simulation data when no rotational resistance is considered are overlaid in Figure 7 for comparison, denoted as NRR. From the onset of shearing, the deviatoric stress is much higher when rotational resistance is considered than when it is ignored (Figure 7(a)). For all the samples, the mobilized stress and volumetric strain becomes constant when the axial strain exceeds 30%, i.e., a critical state is reached as defined within the critical state soil mechanics framework. The angle of shearing resistance ($\phi'$) at the critical state approaches that of Toyoura sand (31°) as $\kappa$ increases, i.e., the compressive strength of the asperities increases (Figure 7(b)). The effect of $\kappa$ is significant when it is below 0.3. However, when $\kappa$ exceeds 0.3, the influence of $\kappa$ on the shear strength is less noticeable and the strength for $\kappa$ = 1 is almost identical to that when no limit is set in the rotational resistance model. This also agrees with Eq. 11 which indicates that the energy dissipation rate (slope of Stage II) increases significantly from $\kappa$=0.1 to $\kappa$=0.5 but is very similar for $\kappa$=0.5 and $\kappa$=1.0. Considering the volumetric response (Figure 7(c)), while the NRR sample is contractive overall, when rotational resistances are considered the samples initially contract but then dilate and are dilative overall. The magnitude of dilation increases with increasing $\kappa$ when $\kappa$ < 0.3; however, for $\kappa$ > 0.3, the samples behave less dilatively as $\kappa$ increases and the volumetric response for $\kappa$ = 1 is close to that for the case when no limit is set for the rotational resistance.

The effect of $\kappa$ on the proportion of the plastic contacts at which the plastic limit of the contact springs is reached is presented in Figure 8. Specifically, the sliding fraction corresponds to the proportion of contacts at which the sliding limit is reached, while the rolling/twisting fraction quantifies the proportion of contacts at which the rolling/twisting limit is reached. The sliding fraction increases when rotational resistance is introduced but oscillations are more obvious in the sliding fraction when rotational resistance is considered as shown in Figure 8(a). The sliding fraction seems to increase with increasing $\kappa$ as the sliding fraction for $\kappa$ = 0.1 is slightly lower than those for $\kappa$ = 0.3 or 1. Plastic yielding of the rolling and twisting springs is considered separately. The rolling fraction decreases dramatically from 0.59 to 0.02 as $\kappa$ is increased from 0.1 to 1 (Figure 8(b)). The twisting fraction also decreases as $\kappa$ increases (Figure 8(c)). The rolling fraction is higher than the twisting fraction when $\kappa$ < 0.3, while for $\kappa$ =1.0, the twisting fraction becomes slightly higher than the rolling fraction. Figure 8 reveals that when $\kappa$ is low, rotational behaviour dominates while the fraction of rolling contacts decreases dramatically when $\kappa$ exceeds 0.3.

The contacts can be further categorised into eight subgroups according to which type of plastic limit (rolling, twisting and sliding) is reached, considering the contact as elastic when none of these plastic

limits are attained. The classifications are as follows: **PR**: pure rolling; **PT**: pure twisting; **PS**: pure sliding; **Elastic**: no rolling, no twisting and no sliding; **R-T**: rolling and twisting; **R-S**: rolling and sliding; **T-S**: twisting and sliding; **R-S-T**: rolling, sliding and twisting. Figure 9 presents the effect of $\kappa$ on the elastic-plastic configurations of the contacts considering three $\kappa$ values ($\kappa$=0.1, 0.3 and 1). The fraction of the elastic contacts decreases immediately after loading commences. The fraction of contacts at which only one type of plastic limit is reached is significantly higher than the fraction of contacts at which more than one type of plastic limit are attained. When $\kappa$ is low ($\kappa$ = 0.1), the PR contact classification is the most common case, while the fraction of the contacts which remain elastic is the second-most significant case (Figure 9(a)). The number of PS contacts is higher than the number of PT contacts. The larger proportion of PR contacts than PT contacts indicates anisotropy in the rotational motion when the rotational resistance is introduced. At the intermediate $\kappa$ value considered (Figure 9(b)), about 53% of the contacts are elastic, the number of PR contacts is close to the number of PS contacts and the difference between the numbers of PR and PT contacts diminishes. When a $\kappa$ value as high as 1 is used (Figure 9(c)), most of the contacts are elastic. The number of PS contacts surpasses the number of either PR or PT contacts. The number of PT contacts exceeds the number of PR contacts, which is due to the decreasing constraints acting on the particles that participate in force transmission as a consequence of the reduced number of lateral supports. Obviously, there is a transition from rolling to sliding at the contacts as $\kappa$ increases which is opposite to the case when the inter-particle friction coefficient is increased systematically in the absence of rotational resistance (Huang et al., 2014).

Similarly, the influence of shape, as expressed by the parameter $\delta$, on the stress–strain behaviour is also non-linear. In accordance with the effects of $\kappa$, the influence of $\delta$ on the overall responses can also been linked to the transition from rolling to sliding and from plastic to elastic at the contacts (Huang, 2014).

### 5.3 Position of the critical state line (CSL)

Figure 10 shows the effect of $\delta$ on the critical-state loci obtained in both $e$-log($p'$) and $q$-$p'$ spaces for $\kappa$=1. The CSL when rotational resistance is not activated (indicated by the black dashed line and denoted as NRR) (Huang et al., 2014) and the CSL for real Toyoura sand (Verdugo and Ishihara, 1996) are superimposed on Figure 10. Figure 10(a) shows that the void ratio at the critical state when rotational resistance is considered is higher than that when rotational resistance is absent. The void ratio at the critical state increases with increasing $\delta$ and the effect of $\delta$ becomes negligible when $\delta$ exceeds 3. Although rotational resistance can increase the void ratio at the critical state, the effect is limited and the critical-state void ratio remains below that for real Toyoura sand. These differences can be attributed to the inability of the DEM with spherical particles to capture the kinematics and moment transfer that occurs in the case of non-spherical particles, as illustrated in Figure 1(a). Figure

10(b) shows that the slope of the CSL in *q-p'* space increases as $\delta$ increases. The effect of $\delta$ is significant when $\delta$ is below 3; again, the effect of $\delta$ becomes negligible when $\delta$ exceeds 3 and the slope of the CSL remains below the value of real Toyoura sand for $\mu = 0.25$ as considered here.

The strength and dilatancy of a DEM assembly can be further enhanced by increasing the inter-particle friction coefficient. However, as discussed in Huang et al. (2014), it is not a physically meaningful approach to match the strength and dilatancy of a real sand by increasing the inter-particle friction coefficient beyond 0.5.

**6. Discussion and Conclusions**

In this study, a rotational resistance model with a physical basis was used to investigate the influence of particle shape on the behaviour of granular materials. The model contains only two parameters: a shape parameter $\delta$ that describes the particle irregularity and a strength parameter $\kappa$ which relates the strength of asperities to the normal force. An equation was derived for the critical timestep when rotational resistance is incorporated in a DEM simulation. This derivation shows that simulation stability can be ensured by using the critical timestep for the case when rotational resistance is absent. The analytical expressions of particle motion for several single-contact scenarios have been derived. These expressions can be employed to check the correctness of the implementation of rotational resistance models including the one used in the current study. The ability of rotational resistance to represent the influence of particle shape on the mechanical behaviour has been discussed.

Both $\kappa$ and $\delta$ have significant effects on the stress-strain behaviour of the numerical assemblies when subjected to triaxial shearing. The strength increases with both $\kappa$ and $\delta$. While the dilative volumetric strain increases consistently with increasing $\delta$, this is only true for $\kappa \leq 0.3$: when $\kappa$ exceeds 0.3, the numerical sample behaves less dilatively. This indicates that surface topology has a more significant influence on interlocking than asperity strength. The nonlinear influence of rotational resistance on the overall mechanical response is linked to the limited effect of rotational resistance on the structural anisotropy and stability of strong force chains.

Rolling has been identified as the dominant behaviour at the contacts for spherical grains (Bardet, 1994; Oda et al., 1982) which is not the case when rotational resistance/particle irregularity is present. There is a transition from rolling to sliding at the contacts as rotational resistance increases. Specifically, rolling is more obvious than sliding when $\kappa$ is small while sliding surpasses rolling when $\kappa$ is further increased. The increase of strength with increasing rotational resistance is due to the increased number of elastic contacts and the associated increased stability of strong force chains.

A comparison of the critical-state loci in both *q-p'* and *e*-log(*p'*) spaces shows that the strength and the void ratio at the critical state are affected by rotational resistance. In particular, the slope of the CSL in *q-p'* space increases as $\delta$ increases. Rotational resistance yields higher void ratios at the critical state than the traditional DEM simulations and the critical-state loci in *e*-log(*p'*) space move upwards as $\delta$ increases. However, the effect of rotational resistance is limited and cannot yield a CSL that is close to the real Toyoura sand composed of sub-angular to angular sand grains in either *q-p'* or *e*-log(*p'*) space. This is possibly because rotational resistance models can only simulate the interlocking effect, while the mechanism of moment resistance that arises when the branch vector orientation differs from the contact normal vector orientation is not captured. The latter will be significant when the surface texture of particles is smooth. As noted by Markauskas and Kacianauskas (2011), DEM simulations can closely capture the real behaviour of granular materials only when both mechanisms are combined. Therefore, future research will be carried out to apply the model proposed here to ellipsoids or simple clusters (agglomerates) of spherical particles.

**Acknowledgements**

Computational time on HECToR was provided as part of grant EP/I006761/1 from the Engineering and Physical Sciences Research Council. Access to the HPC facility cx1, provided by Imperial College London, is highly appreciated. The funding support from the National Natural Science Foundation of China (Grant No. 51509186) is also appreciated.

**References**


Ai, J., Chen, J.-F., Rotter, J.M. & Ooi, J.Y. (2011). Assessment of rolling resistance models in discrete element simulations. *Powder Technology*, 206, 269–282.

Bardet, J.P. (1994). Observations on the effects of particle rotations on the failure of idealized granular materials. *Mechanics of Materials*, 18, 159–182.

Belytschko, T. (1983). An overview of semidiscretization and time integration procedures, in: Belytschko, T. and Hughes, T.J.R. (Ed.), Computational Methods for Transient Analysis, Computational Methods in Mechanics Series. North Holland, New York, NY.

Cavarretta, I., Coop, M. & O'Sullivan, C. (2010). The influence of particle characteristics on the behaviour of coarse grained soils. *Géotechnique*, 60(6), 413-423.

Calvetti, F. (2008) Discrete modelling of granular materials and geotechnical problems. *European Journal of Environmental and Civil Engineering*, 12(7-8), 951-965.

Cho, G., Dodds, J. & Santamarina, J. (2006). Particle shape effects on packing density, stiffness, and strength: natural and crushed sands. *Journal of Geotechnical and Geoenvironmental Engineering*, 132, 591–602.

Garcia, X., Latham, J.-P., Xiang, J. & Harrison, J.P. (2009). A cluster overlapping shpere algorithm to represent real particles in discrete element modelling. *Géotechnique*, 59(9), 779-784.

Golub, G.H. & Van Loan, C.F. (1983). Matrix-Computations. North Oxford Academic, Oxford.

Huang, X. (2014). Exploring critical-state behaviour using DEM. PhD Thesis, The University of Hong Kong & Imperial College London.

Huang, X., Hanley, K., O'Sullivan, C. & Kwok, C.Y. (2014). Exploring the influence of inter-particle friction on critical state behaviour using DEM. *International Journal of Numerical and Analytical Methods in Geomechanics*, 38, 1276–1297.

Itasca Consulting Group (2007). PFC3D Version 4.0 User Manual. Itasca Consulting Group, Minneapolis, MN, USA.

Iwashita, K. & Oda, M. (1998). Rolling resistance at contacts in simulation of shear band development by DEM. *Journal of Engineering Mechanics*, 124, 285–292.

Jessen, R.P., Bosscher, P.J., Plesha, M.E. & Tuncer B.E. (1999). DEM simulation of granular media-structure interface: Effects of surface roughness and particle shape. *International Journal for Numerical and Analytical Methods in Geomechanics*, 23(6), 531-547

Jiang, M.J., Yu, H.-S. & Harris, D. (2005). A novel discrete model for granular material incorporating rolling resistance. *Computers and Geotechnics*, 32, 340–357.

Jiang, M.G., Shen, Z.F. & Wang, J.F. (2015). A novel three-dimensional contact model for granlulates incorporating rolling and twisting resistance. *Computers and Geotechnics*, 65, 147–163.

Johnson, K. (1985). Contact Mechanics, First. ed. Cambridge University Press, Cambridge, United Kingdom.

Markauskas, D. & Kacianauskas, R. (2011). Investigation of rice grain flow by multi-sphere particle model with rollilng resistance. *Granular Matter*, 13: 143-148.

Mohamed, A. & Gutierrez, M. (2010). Comprehensive study of the effects of rolling resistance on the stress–strain and strain localization behavior of granular materials. *Granular Matter*, 12, 527–541.

Oda, M. & Kazama, H. (1998) Microstructure of shear bands and its relation to the mechanisms of dilatancy and failure of dense granular soils. *Géotechnique*,48(4), 465-481.

Oda, M., Konishi, J. & Nemat-Nasser, S. (1982). Experimental micromechanical evaluation of strength of granular materials: effects of particle rolling. *Mechanics of Materials*, 1, 269–283.

O'Sullivan, C. & Bray, J.D. (2004). Selecting a suitable time step for discrete element simulations that use the central difference time integration scheme. *Engineering Computations*, 21, 278–303.

Otsubo, M., O'Sullivan, C., Sim, W.W. & Ibraim, E. (2015). Quantitative assessment of the influence of surface roughness on soil stiffness. *Géotechnique*, 65(8), 694-700

Payan M., Khoshghalb A., Senetakis K. & Khalili N. (2016a). Small-strain stiffness of sand subjected to stress anisotropy. *Soil Dynamics and Earthquake Engineering*, 88, 143 - 151

Payan M., Senetakis K., Khoshghalb A., Khalili N. (2016b). Influence of particle shape on small-strain damping ratio of dry sands. *Géotechnique*, 66(7), 610 - 616

Plassiard, J.-P., Belheine, N. & Donzé, F.-V. (2009). A spherical discrete element model: calibration procedure and incremental response. *Granular Matter*, 11, 293–306.

Plimpton, S. (1995). Fast parallel algorithms for short-range molecular dynamics. Journal of Computational Physics, 117, 1–19.

Senetakis, K., Coop, M.R., Todisco, M.C. (2013). Tangential load–deflection behaviour at the contacts of soil particles. *Géotechnique Letters*, 3(2), 59–66

Shin, H. & Santamarina, J.C. (2013). Role of Particle Angularity on the Mechanical Behavior of Granular Mixtures. *Journal of Geotechnical and Geoenvironmental Engineering*, 139, 353–355.

Thomas, P.A. & Bray, J.D. (1999). Capturing nonspherical shape of granular media with disk clusters. *Journal of Geotechnical and Geoenvironmental Engineering*, 125(3), 169-178

Thornton, C. (2000). Numerical simulations of deviatoric shear deformation of granular media. *Géotechnique*, 50, 43–53.

Thornton, C., Cummins, S.J. & Cleary, P.W. (2013). An investigation of the comparative behaviour of alternative contact force models during inelastic collisions. *Powder Technology*, 233, 30–46.

Tordesillas, A. & Walsh, D.C.S. (2002). Incorporating rolling resistance and contact anisotropy in micromechanical models of granular media. *Powder Technology*, 124, 106–111.

Verdugo, R. & Ishihara, K. (1996). The steady state of sandy soils. *Soils and Foundations*, 36, 81–91.

Yang, J. & Wei, L.M. (2012). Collapse of loose sand with the addition of fines : the role of particle shape. *Géotechnique*, 62, 1111–1125.

Yang, Z.X., Yang, J. & Wang, L.Z. (2012). On the influence of inter-particle friction and dilatancy in granular materials: a numerical analysis. *Granular Matter*, 14, 433–447.

Zhang, H. & Makse, H. (2005). Jamming transition in emulsions and granular materials. Phys. Rev. E 72, 1–12.

Zhao, J. & Guo, N. (2014). Rotational resistance and shear-induced anisotropy in granular media. *Acta Mechanica Solida Sinica*, 27, 1–14.

Zhou, Y.C., Wright, B.D., Yang, R.Y., Xu, B.H. & Yu, A.B. (1999). Rolling friction in the dynamic simulation of sandpile formation. *Physica A Statistical Mechanics & Its Applications*, 269, 536–553.

**Figures**

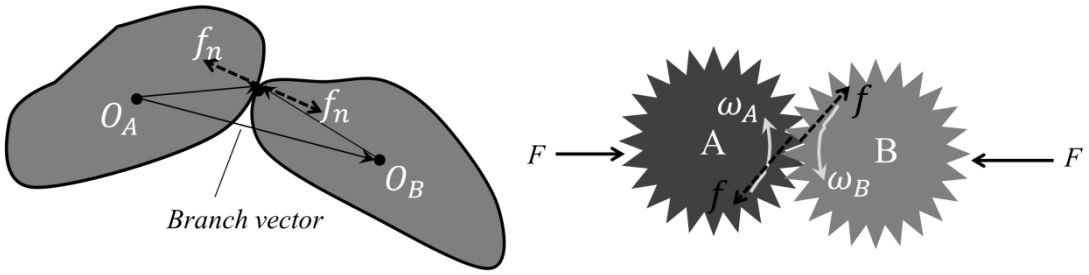


(a) (b)

Figure 1 Illustration of the physical origin of rotational resistance: (a) Noncoincidence between the branch vector direction and the contact normal direction; (b) Interlocking effect

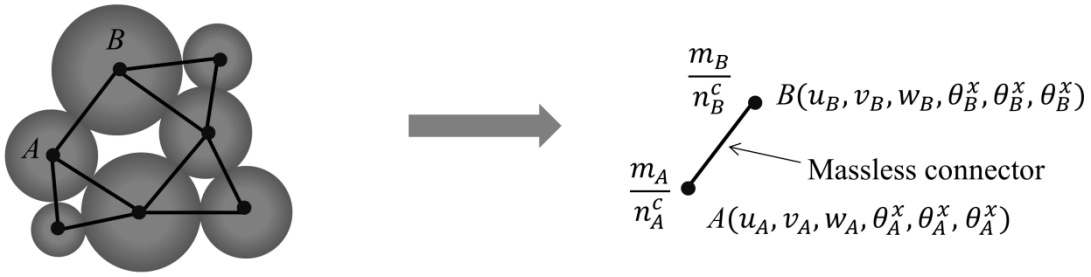


(a)

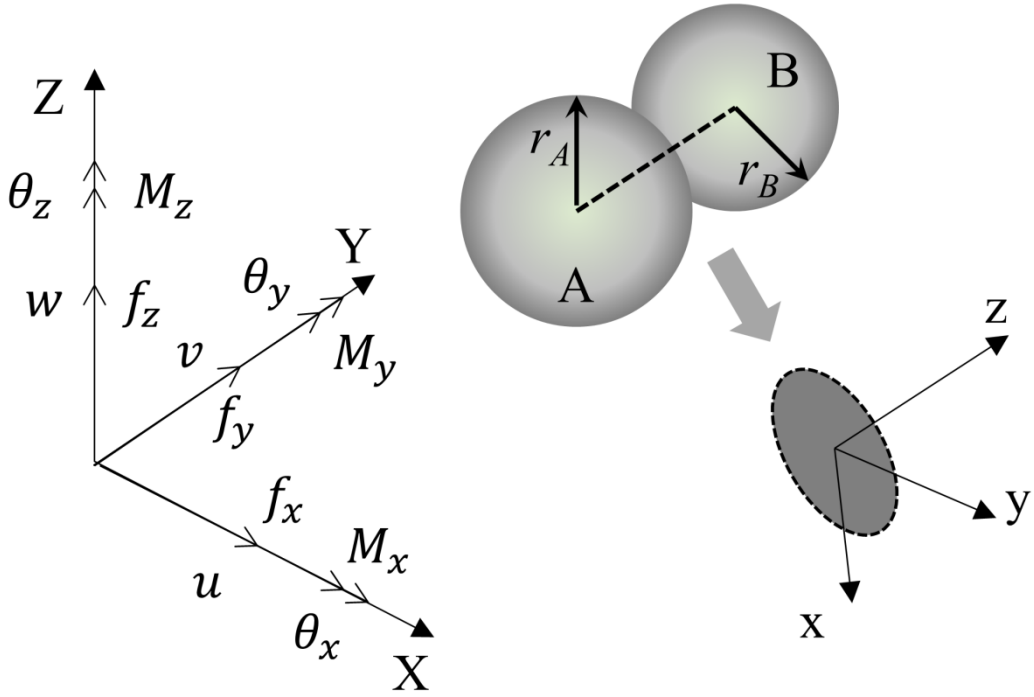


(b)

Figure 2 Schematic illustration of: (a) the construction of the lumped mass matrix; (b) the local and global coordinate system for two particles in contact

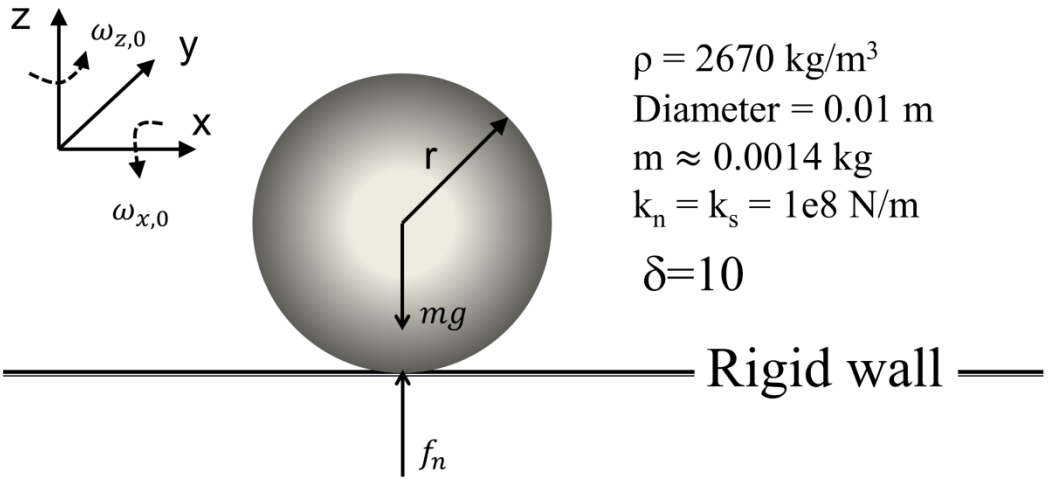


(a)

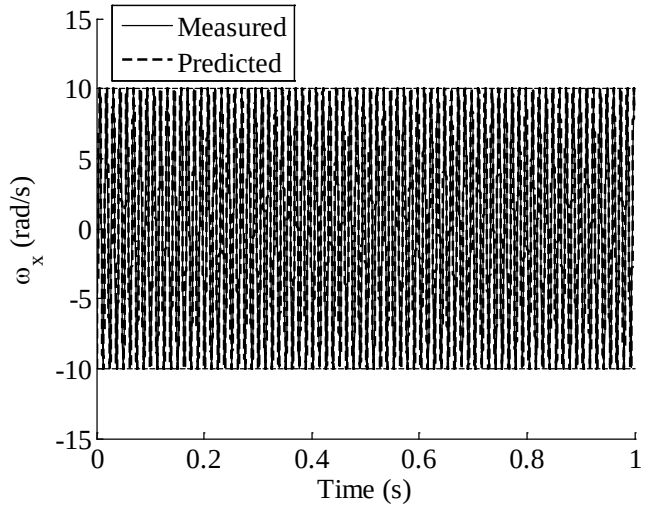


(b)

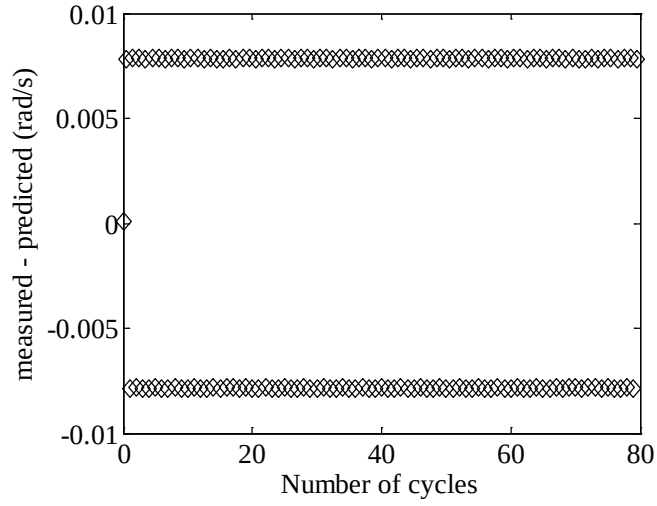


(c)

Figure 3 A single particle spins on a frictionless flat rigid wall: (a) Sketch of the model; (b) Comparison between the measured motion and the analytical harmonic motion (Δt = 1e-6, no limit on the rolling resistance); (c) Difference between the measured $\omega_x$ and the predicted $\omega_x$ at the peak and the valley

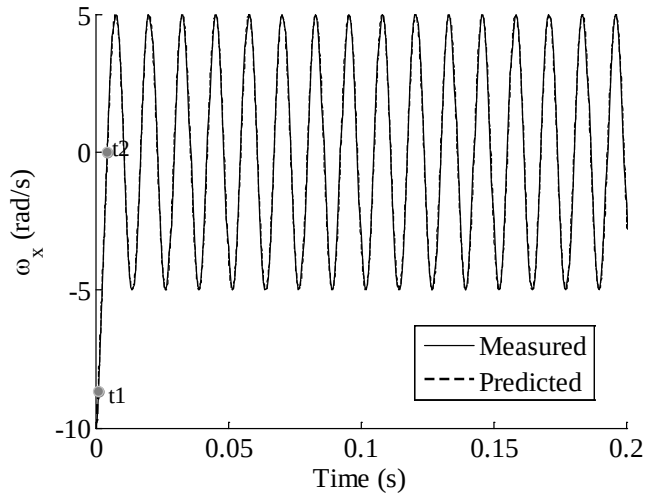


(a)

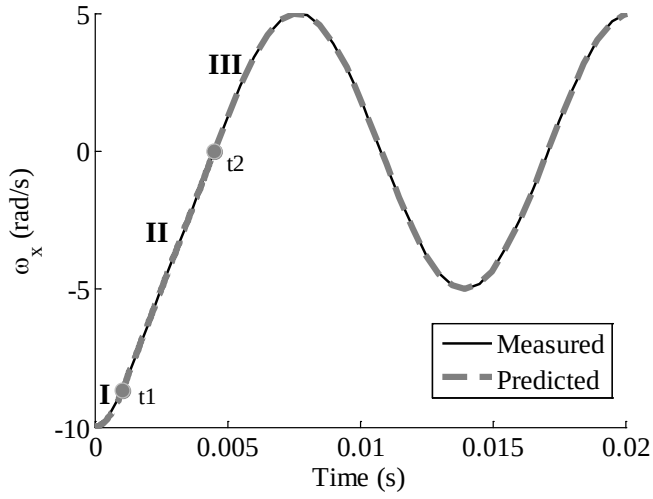


(b)

Figure 4 Comparison between the measured motion and the theoretically-derived motion when the rolling resistance is bounded by a limit (κ=0.5): (a) between 0 and 0.2 s; (b) between 0 and 0.02 s

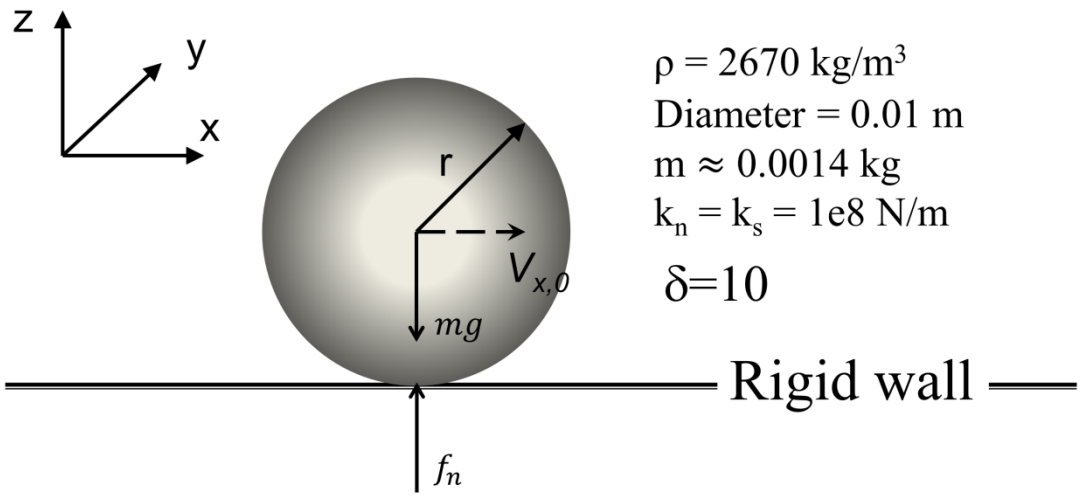


(a)

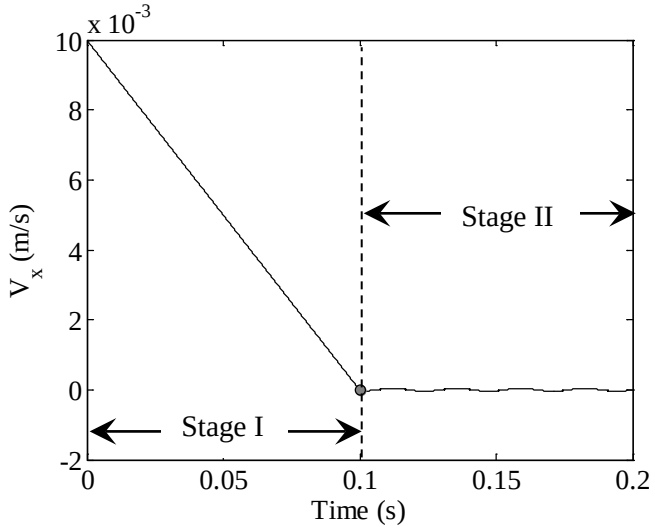


(b)

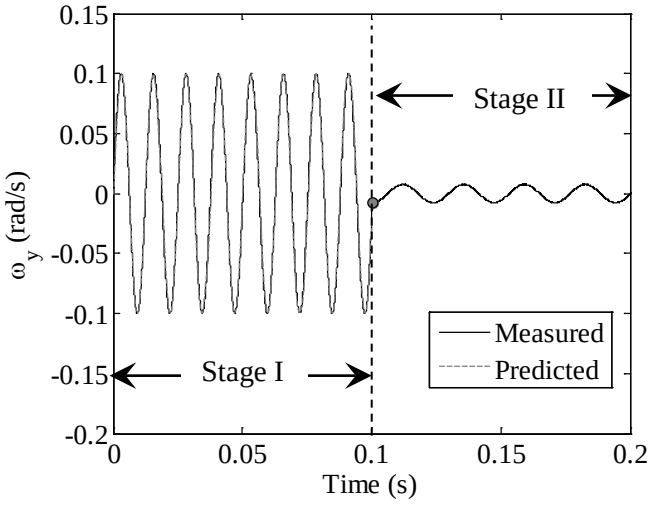


(c)

Figure 5 The kinematics of a single ball moving along a flat wall with initial translational velocity: (a) illustration of the model; (b) Translational velocity; (c) Rotational velocity

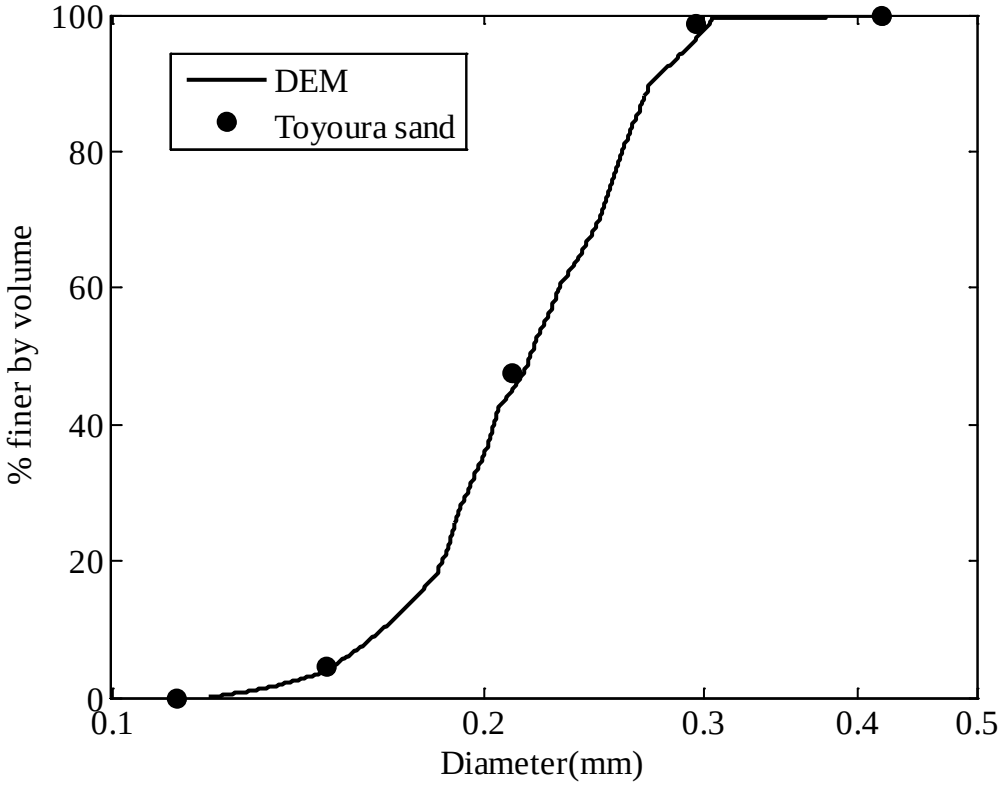


Figure 6 Comparing the particle size distribution (PSD) curve of the numerical assembly and Toyoura sand

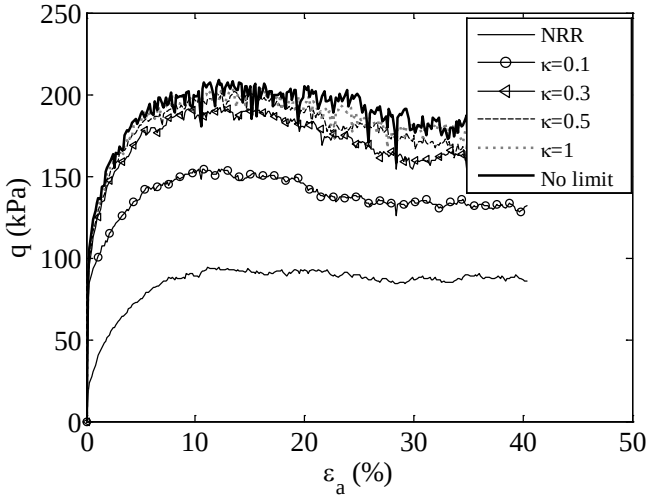


(a)

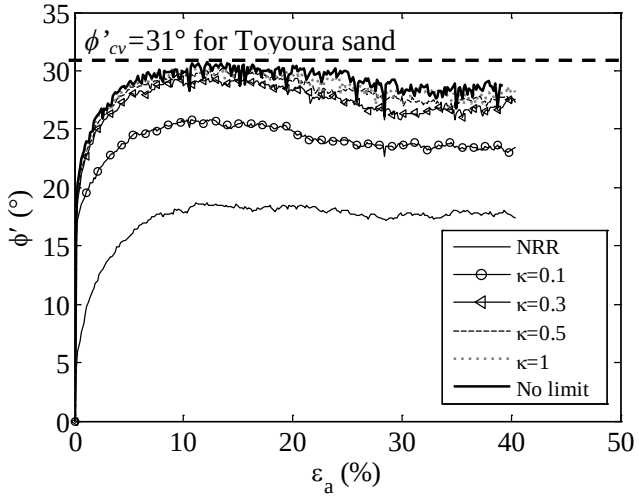


(b)

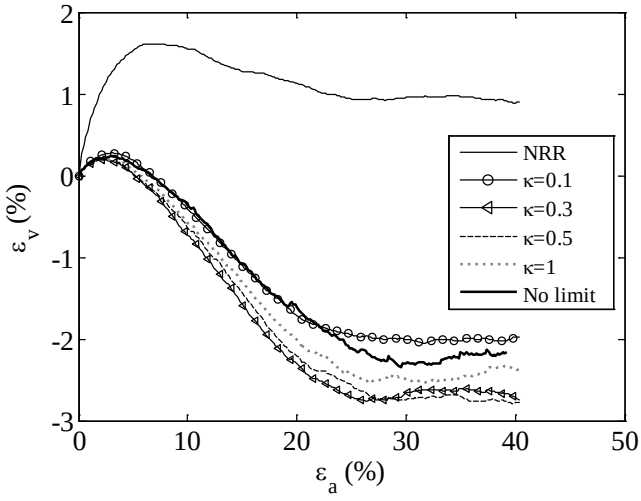


(c)

Figure 7 Influence of $\kappa$ on the mechanical behaviour ($e_0$=0.646, $\sigma'_3$=100 kPa, NRR denotes no rotational resistance): (a) Deviatoric stress vs axial strain; (b) Angle of shearing resistance vs axial strain; (c) Volumetric strain vs axial strain

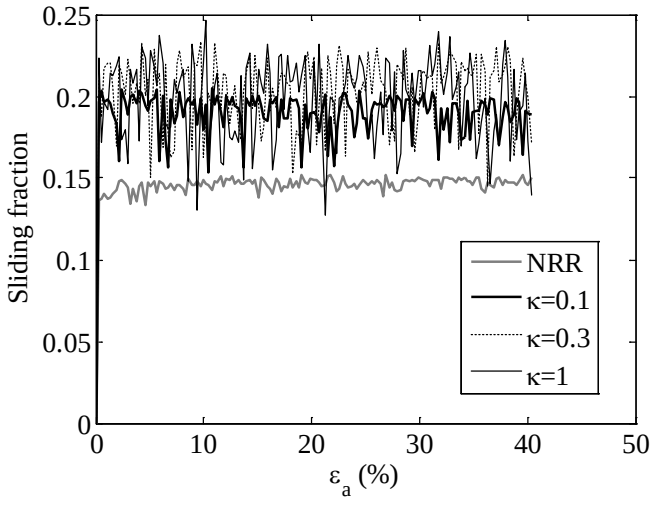


(a)

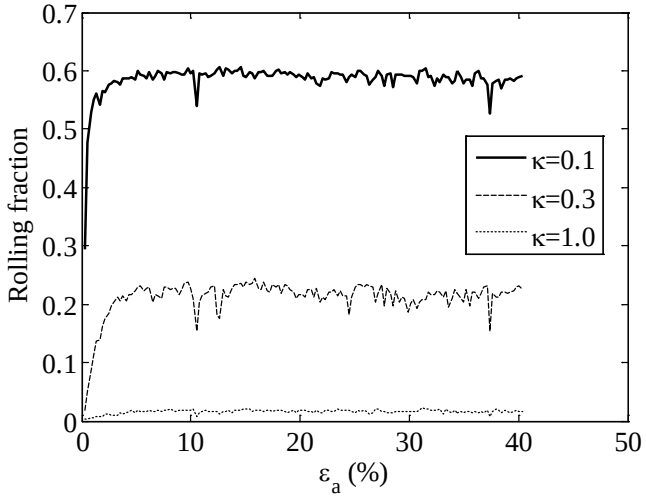


(b)

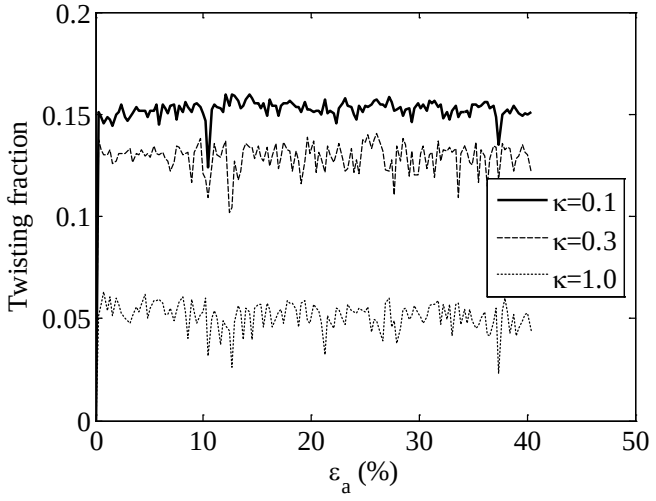


(c)

Figure 8 Influence of $\kappa$ on the fraction of the contacts that reach the plastic limit: (a) Sliding fraction; (b) Rolling fraction; (c) Twisting fraction

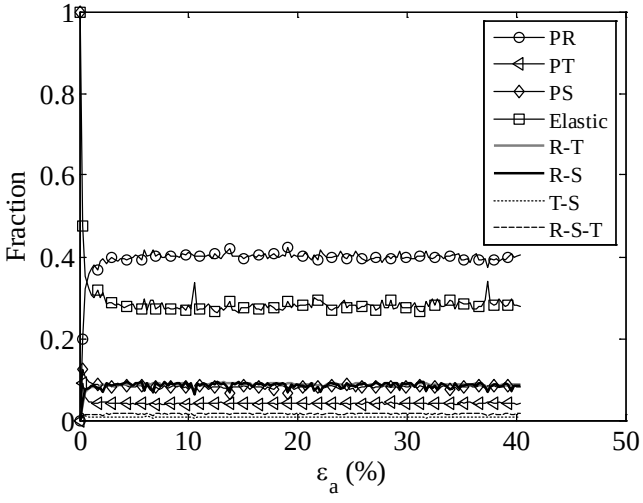


(a)

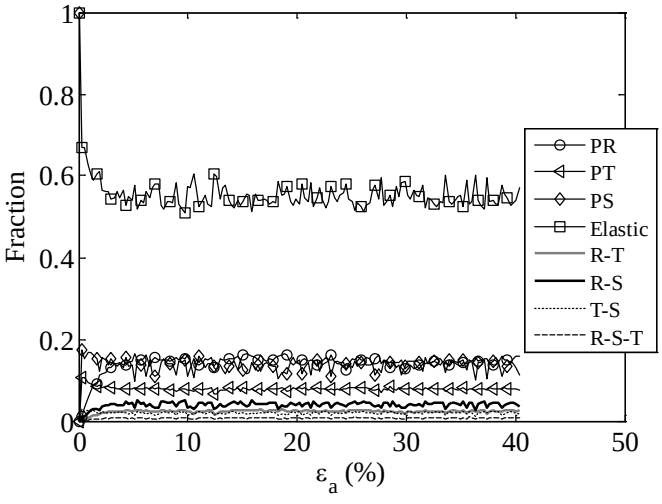


(b)

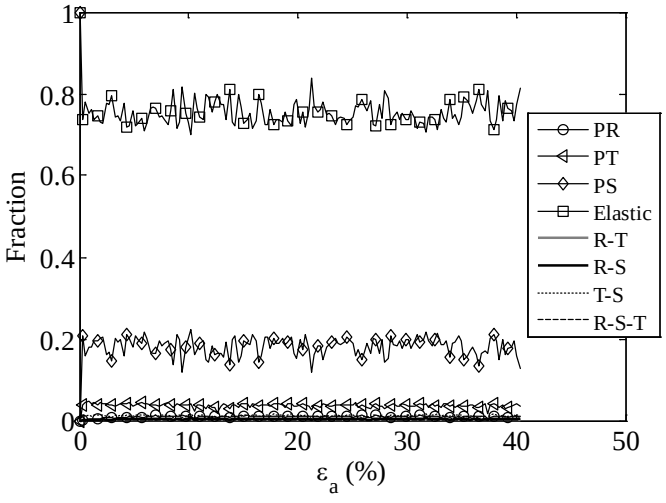


(c)

Figure 9 Effects of $\kappa$ on the elastic and plastic configurations of the contacts: (a) $\kappa$=0.1; (b) $\kappa$=0.3; (c) $\kappa$=1 (**PR**: pure rolling; **PT**: pure twisting; **PS**: pure sliding; **Elastic**: no rolling, no twisting and no sliding; **R-T**: rolling and twisting; **R-S**: rolling and sliding; **T-S**: twisting and sliding; **R-S-T**: rolling, sliding and twisting)

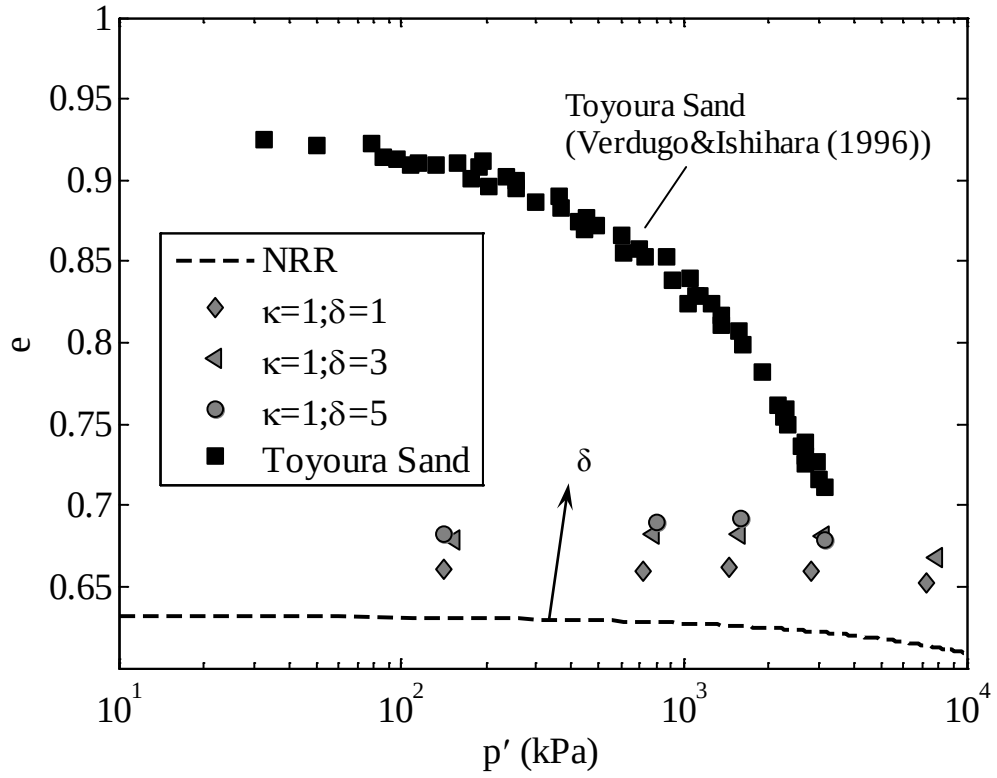


(a)

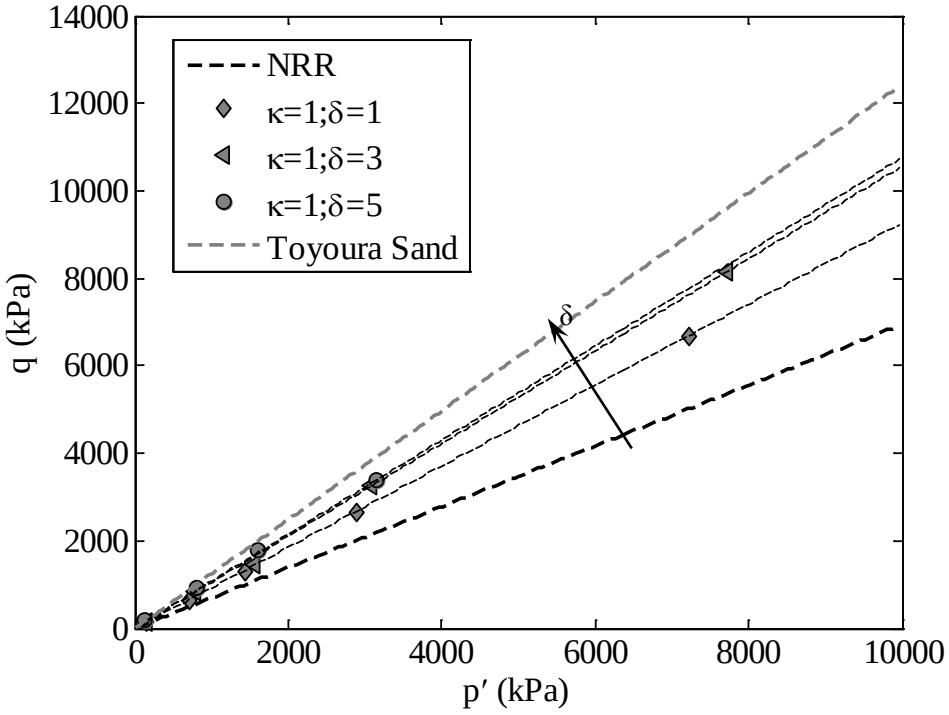


(b)

Figure 10 Effect of rotational resistance on the position of the critical state lines: (a) *e*-log(*p'*) space; (b) *q*-*p'* space

**Supplementary material: derivation of the rotational resistance model**

**Basic assumptions**

The rotational resistance model proposed herein is derived based on the following assumptions:

- The interaction between two contacting particles occurs over a finite circular contact area
- The contact is idealised to be composed of uniformly-distributed elastic springs in both the normal and tangential directions as shown in Figure A. The mean contact stiffnesses ($\bar{k}_n$ and $\bar{k}_s$) of the equivalent springs distributed over the contact area can be derived by equating the integrated contact forces ($f_n$ and $f_t$) over the entire contact area to that calculated from a single spring system ($k_n$ and $k_s$) by:

$$f_n = k_n U_n = \int_0^{2\pi}\int_0^B (\bar{k}_n \cdot U_n)\cdot(r\cdot dr\cdot d\varphi) = \bar{k}_n \cdot U_n \cdot \pi B^2 \qquad \text{(Eq. A1)}$$

$$\Delta f_t = k_s \Delta s = \int_0^{2\pi}\int_0^B (\bar{k}_s \cdot \Delta s)\cdot(r\cdot dr\cdot d\varphi) = \bar{k}_s \cdot \Delta s \cdot \pi B^2 \qquad \text{(Eq. A2)}$$

where $U_n$ is the contact overlap, $\Delta f_t$ is the tangential force increment, $\Delta s$ is the incremental tangential displacement and $B$ is the radius of the contact plane. Therefore $\bar{k}_n = k_n/A$ and $\bar{k}_s = k_s/A$, where $A = \pi B^2$ is the area of the circular contact plane.

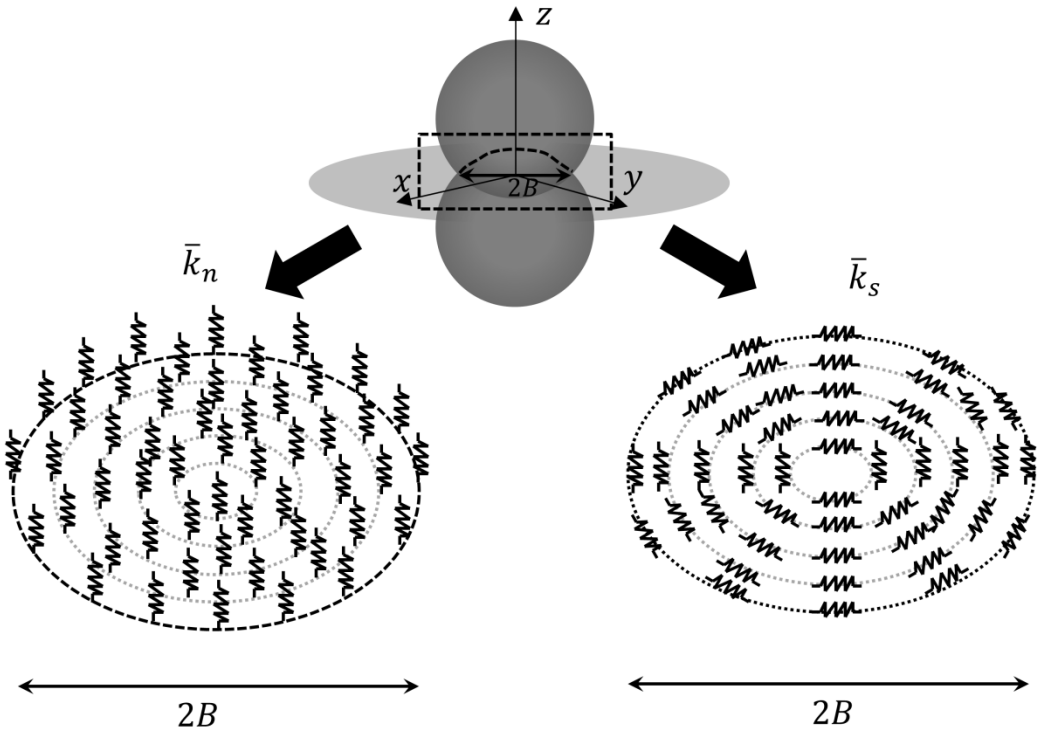


Figure A Discretisation of the contact springs

**Derivation of the rolling resistance model**

Rolling is the relative angular velocity between the two bodies about an axis lying in the contact plane. For the idealised model illustrated in Figure B, when two touching particles have the tendency to roll against each other about an axis in the contact plane (for example the *x* or the *y* axis as illustrated here), the normal contact springs towards the front of the contact area in the relative rotation direction will be extended while the contact springs towards the rear of the contact area will be compressed (Figures B (a) and (b)). Therefore, the rotational resistance $M_r^i$ $(i = x, y)$, which acts to oppose the relative rotation, results from the uneven distribution of the normal contact force and can be determined by:

$$M_r^i = \int_0^{2\pi}\int_0^B (r \cdot cos\varphi) \cdot (\bar{k}_n \cdot r \cdot \theta_r^i \cdot dr \cdot r \cdot d\varphi) = \bar{k}_n \frac{\pi}{4} B^4 \theta_r^i = \bar{k}_n I_i \theta_r^i \ \ (i = x, y) \quad \text{(Eq. A3)}$$

in which $I_i = \frac{\pi}{4}B^4$ is the area moment of inertia of a circular area with respect to the $i^{\text{th}}$ axis in the contact plane and $\theta_r^i$ is the relative rotation angle around the $i^{\text{th}}$ axis. Eq. A3 indicates that the rolling stiffness $k_r = \bar{k}_n I_i$. The contact opens when the relative angular displacement exceeds a limit value $\theta_r^m = \tan^{-1}(\frac{U_n}{B})$ as shown in Figure B (c).

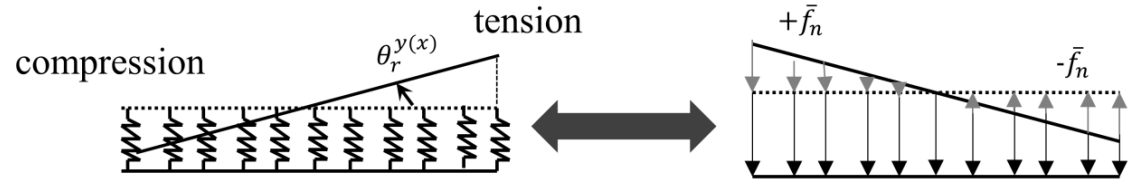


(a)

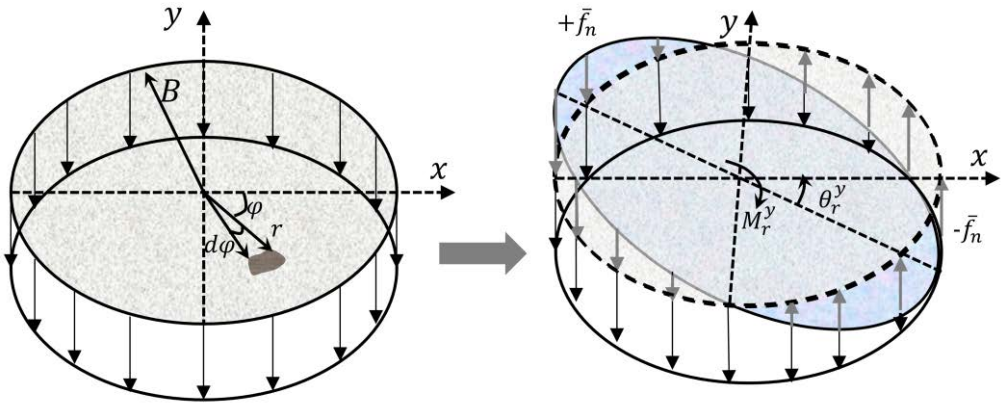


(b)

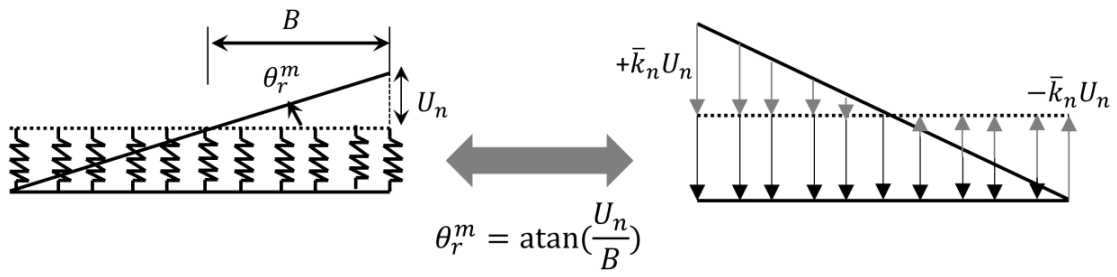


(c)

Figure B Assumed mechanism of rolling resistance: (a) 2D illustration; (b) 3D illustration of contact force redistribution due to rolling about the y axis; (c) Limit of the rolling resistance prior to the opening of the contact

*Relative rotation*

According to Oda et al. (1982), there are three mechanisms of relative displacement between two touching particles: pure rolling, pure sliding and rolling-sliding. The pure rolling and pure sliding cases are illustrated in Figure C. In pure rolling (Figure C (a)), the incremental traces of the contact point on the two particle surfaces are the same in magnitude but opposite in direction ($\widehat{cc_1} = -\widehat{cc_2}$), while $\widehat{cc_1}/r_1 = \widehat{cc_2}/r_2$ for pure sliding (Figure C (b)). Pure rolling and pure sliding are special cases; for most contacts rolling and sliding occur concurrently or successively (Bardet, 1994; Iwashita and Oda, 1998). Determination of the relative rotation, $\theta_r^i$ , here has followed Bardet (1994) and Jiang et al. (2005). Figure D shows the kinematics of two touching particles from time step *t*-*Δt* to time step *t*, where *z* is parallel to the contact normal at the time step *t*. The incremental traces of the contact point on particle *i* and particle *j*, *da* and *db* respectively, can be given by:

$$\begin{cases} da = \widehat{c'c'_1} = r_1(d\theta_1 - d\alpha) \\ db = \widehat{c'c'_2} = r_2(d\theta_2 - d\alpha) \end{cases} \quad \text{(Eq. A4)}$$

where $r_1$ and $r_2$ are the radii of particle $i$ and particle $j$ respectively, $d\theta_1$ and $d\theta_2$ are the incremental angles between $O_1O_2$ and $O'_1c'_1$ and between $O_1O_2$ and $O'_2c'_2$ and $d\alpha$ is the incremental change of the contact direction with reference to the local coordinate system, taking counter-clockwise rotation as positive. The relative displacement increment $dU_s$ and the rolling component of the relative displacement ($dU_r$) can be used to determine *da* and *db* as:

$$\begin{cases} da = m_1 dU_s + m_2 dU_r \\ db = m_3 dU_s + m_4 dU_r \end{cases} \quad \text{(Eq. A5)}$$

where $m_1$ and $m_3$ denote the proportions of the sliding component of relative displacement that contribute to *da* and *db* respectively, while $m_2$ and $m_4$ quantify the proportions of the

rolling component that contribute relative displacement to *da* and *db* respectively. Eq. A6 and A7 describe the pure rolling condition and the pure sliding condition respectively as follows

$$\begin{cases} d\alpha = 0,\ d\theta_1 = -\frac{r_2}{r_1} d\theta_2, da = -db \neq 0 \\ dU_s = 0, dU_r = da = r_1\theta_1 \end{cases} \quad \text{(Eq. A6)}$$

$$\begin{cases} d\theta_1 = d\theta_2 = 0, da = \frac{r_1}{r_2} db \\ dU_r = 0, dU_s = da + db \end{cases} \quad \text{(Eq. A7)}$$

Substituting Eq. A6 and Eq. A7 into Eq. A5, the four coefficients ($m_1$=$\frac{r_1}{r_1+r_2}$, $m_2 = 1$, $m_3$= $\frac{r_2}{r_1+r_2}$ and $m_4 = -1$) can be obtained, from which and so $dU_r$ and $dU_s$ can be expressed as:

$$\begin{cases} dU_r = \frac{r_2 da - r_1 db}{r_1+r_2} \\ dU_s = da + db \end{cases} \quad \text{(Eq. A8)}$$

Therefore, the incremental relative rotation can be found by Eq. A9:

$$d\theta_{ri} = d\theta_{1i} - d\theta_{2i} = \frac{dU_{ri}}{r_1} - \frac{-dU_{ri}}{r_2} = \frac{dU_{ri}}{\frac{r_1 r_2}{r_1+r_2}},\ i = x, y \quad \text{(Eq. A9)}$$

which naturally gives the rolling radius $R_r = \frac{r_1 r_2}{r_1+r_2}$.

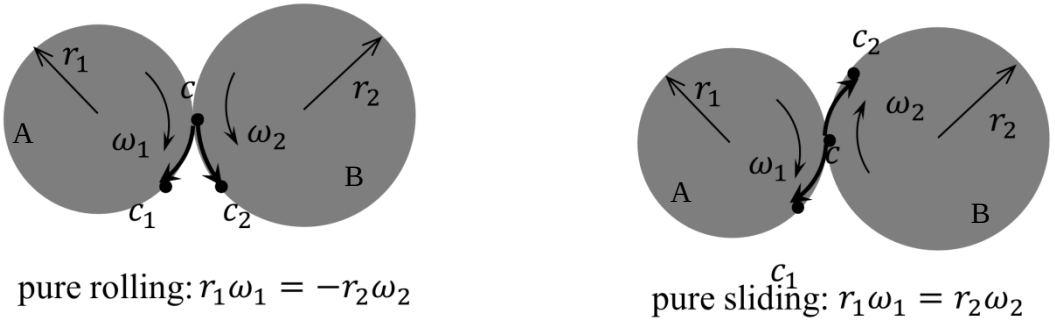


(a) (b)

Figure C Illustration of pure rolling and pure sliding in the absence of rigid-body rotation

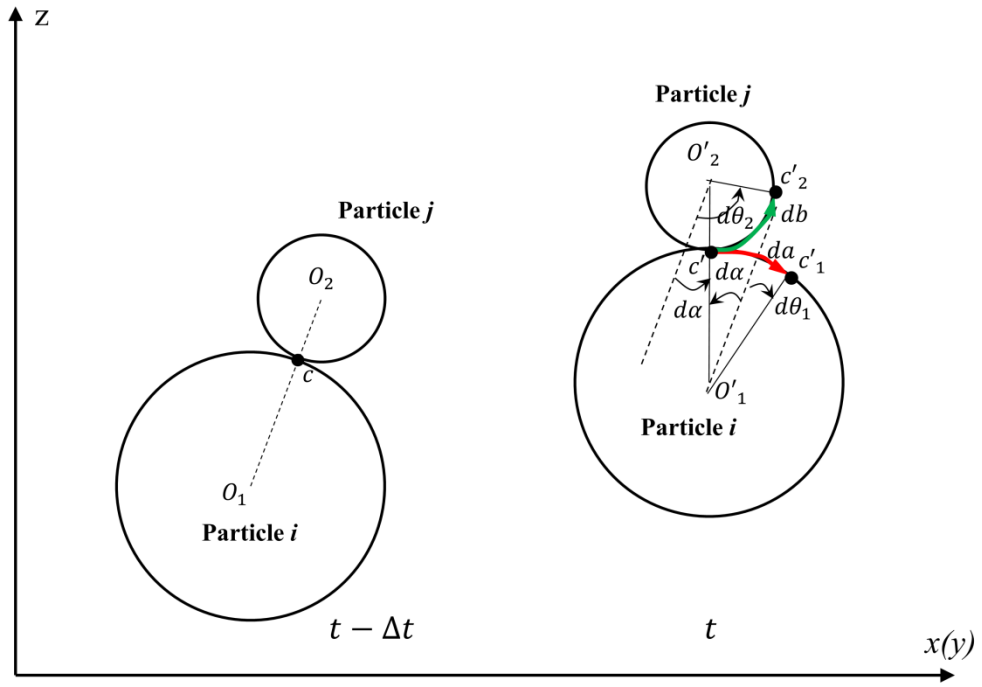


Figure D Kinematics of two particles in contact over a single timestep projected in a local coordinate system (After Jiang et al. (2005))

**Derivation of the twisting resistance model**

Spinning/twisting is the other type of relative angular motion between touching bodies that needs to be considered for three-dimensional problems. The axis of spinning is aligned with the contact normal ***n*** (Duran, 2000; Johnson, 1985). The twisting resistance component of the model is also built up on the spring system illustrated in Figure A. With a finite relative spinning movement $\theta_t$ (Figure E (a)) the annularly-distributed springs will deform to generate annularly-shaped regions of equal shear stress on the contact plane (Figure E (b)). The magnitude of the shear stress ($\tau = \bar{k}_s \cdot r \cdot \theta_t$) is proportional to the radial distance ($r$) between the tangential spring at that point and the centre of the contact plane. As illustrated in Figures E (c) and (d), the annular shear stress results in a torque that acts to oppose the spinning motion which can be expressed by:

$$M_t = \int_0^{2\pi} \int_0^B r \cdot (\bar{k}_s \cdot r \cdot \theta_t \cdot r \cdot d\varphi \cdot dr) = \bar{k}_s \cdot \frac{\pi}{2} B^4 d\theta_z = \bar{k}_s \cdot J_z \cdot \theta_t \qquad \text{(Eq. A10)}$$

in which $J_z = \frac{\pi}{2} B^4$ is the polar area moment of inertia with respect to the $z$ axis. Note that due to axisymmetry, the annular shear stress flow does not induce additional tangential force.

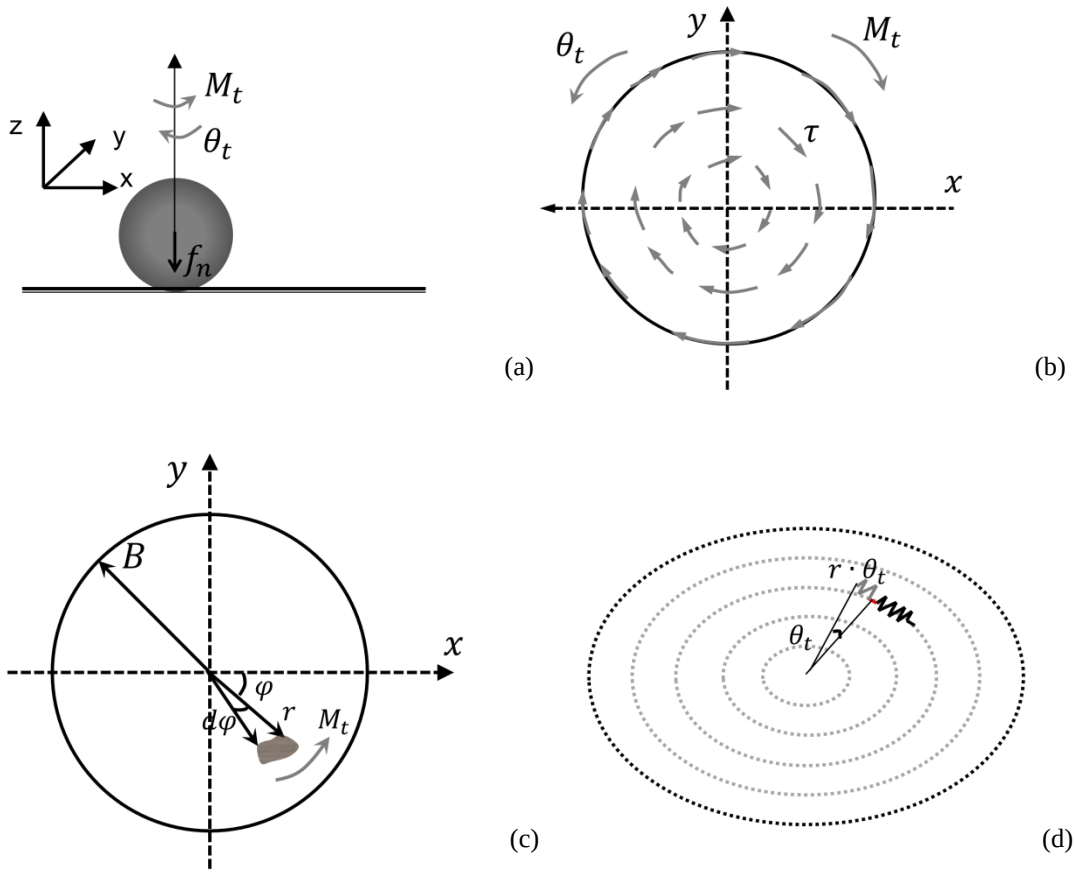


Figure E Assumed mechanism for the twisting/torque resistance model: (a) Kinetic model; (b) Illustration of the annular shear stress flow on the contact plane; (c) and (d) Illustration of the integration element for the calculation of the annular shear stress

Note that derivation of Equations A3-A10 is based on the local coordinate system (*x*-*y*-*z*) with the *z* axis coinciding with the contact normal. Since the directional quantities in LAMMPS are stored in the global coordinate frame (X-Y-Z) and the integration of the governing equations and the contact force calculation are also based on the global coordinate system, a transformation between the two systems are necessary. At the beginning of each timestep, for individual contacts, the calculated global relative angular motion increments ( $d\theta_I = \omega_I \Delta t, I = X, Y, Z$) are transformed to get the relative angular motion increments ($d\theta_i, i = x, y, z$) in the local coordinate system to calculate the local rolling and twisting resistance increments ($dM_i, i = x, y, z$) which are then transformed to the global equivalents ($dM_I, I = X, Y, Z$). Coordinate transformations are performed using quaternions in the current study as the corresponding intrinsic function is available in LAMMPS.

**Quaternion and coordinate transformation**

In mechanical problems, the rotation of the coordinate system is encountered quite frequently, e.g., calculation of the principal stresses. Usually this is achieved by introducing a rotation matrix. However, when a rotation matrix is used, the axes may be no longer orthogonal due to accumulated round-off errors, which may induce quite significant errors when performing coordinate transformation. This can be avoided by using unit quaternions. A quaternion ($\boldsymbol{q} = b + a_x\boldsymbol{i} + a_y\boldsymbol{j} + a_z\boldsymbol{k}$) can be conveniently envisioned as either, a) a vector with four components; b) a scalar plus a vector with three components; or c) a complex number with three different "imaginary" parts.

- Quaternions and spatial rotation

A rotation with an angle $\theta$ around the axis defined by a unit vector $\boldsymbol{u} = u_x\boldsymbol{i} + u_y\boldsymbol{j} + u_z\boldsymbol{k}$ is represented by a quaternion**:**

$$\boldsymbol{q} = cos\left(\frac{1}{2}\theta\right) + \left(u_x\boldsymbol{i} + u_y\boldsymbol{j} + u_z\boldsymbol{k}\right)sin(\frac{1}{2}\theta) \qquad \text{(Eq. A11)}$$

where $\theta$ is the rotation angle which takes counter-clockwise rotation as positive.

As shown in Figure F (a), an ordinary vector $\boldsymbol{p}$ can be treated as a special quaternion with zero real part, i.e., $\boldsymbol{p} = p_x\boldsymbol{i} + p_y\boldsymbol{j} + p_z\boldsymbol{k}$. The new position (**p'**) of $\boldsymbol{p}$ after rotating around a vector $\boldsymbol{u} = u_x\boldsymbol{i} + u_y\boldsymbol{j} + u_z\boldsymbol{k}$ by $\theta$ can be obtained by the conjugation of $\boldsymbol{p}$ by $\boldsymbol{q}$:

$$\boldsymbol{p'} = \boldsymbol{qpq^{-1}} \qquad \text{(Eq. A12)}$$

where

$$\boldsymbol{q^{-1}} = cos\left(\frac{1}{2}\theta\right) - \left(u_x\boldsymbol{i} + u_y\boldsymbol{j} + u_z\boldsymbol{k}\right)sin(\frac{1}{2}\theta) \qquad \text{(Eq. A13)}$$

Unit quaternions, also known as versors, provide a convenient mathematical notation for representing orientations and rotations of objects in three dimensions. Compared to Euler angles, they are simpler to compose and can avoid the problem of gimbal lock, which occurs when the axes of two of the three gimbals are driven into a parallel configuration, "locking" the system into rotation in a degenerate two-dimensional space.

The basic form of a unit quaternion can be described as:

$$\begin{cases} \boldsymbol{q} = q_0 + q_1\boldsymbol{i} + q_2\boldsymbol{j} + q_3\boldsymbol{k} \\ q_0^2 + q_1^2 + q_2^2 + q_3^2 = 1 \end{cases} \qquad \text{(Eq. A14)}$$

If there are several rotation events followed by one another, the new position of $\boldsymbol{p}$ after rotation can be described by:

$$\boldsymbol{p'} = \boldsymbol{q_n \cdots q_1 p q_1^{-1} \cdots q_n^{-1}} \qquad \text{(Eq. A15)}$$

where $\boldsymbol{q_1}$ to $\boldsymbol{q_n}$ are unit quaternions for the *1st* to the *nth* rotations. Thus, we have the equivalent quaternion to combine arbitrary numbers of rotation to be a single rotation using the equivalent quaternion $\boldsymbol{q' = q_n \cdots q_1}$.

- Quaternion and rotation matrix

The use of unit quaternions to account for one time rotation of *Z* axis as shown in Figure F (b) is described below.

The old axes can be described in quaternion form as $\boldsymbol{OX} = 1\boldsymbol{i} + 0\boldsymbol{j} + 0\boldsymbol{k}$, $\boldsymbol{OY} = 0\boldsymbol{i} + 1\boldsymbol{j} + 0\boldsymbol{k}$ and $\boldsymbol{OZ} = 0\boldsymbol{i} + 0\boldsymbol{j} + 1\boldsymbol{k}$. The right-hand rule is used. Therefore, the rotation angle between the old and new *Z* axes is obtained by:

$$\theta = arcsin\left(\frac{|\boldsymbol{OZ} \times \boldsymbol{Oz}|}{|\boldsymbol{OZ}| \cdot |\boldsymbol{Oz}|}\right) \quad \text{(Eq. A16)}$$

while the rotation axis is the cross product of the old and new Z axes:

$$\boldsymbol{u} = \boldsymbol{OZ} \times \boldsymbol{Oz} \quad \text{(Eq. A17)}$$

The unit vector of the rotation axis is given by $\boldsymbol{u} = u_X\boldsymbol{i} + u_Y\boldsymbol{j} + u_Z\boldsymbol{k}$. Hence, the corresponding unit quaternion accounting for such a rotation is:

$$\boldsymbol{q} = q_0 + q_1\boldsymbol{i} + q_2\boldsymbol{j} + q_3\boldsymbol{k} \quad \text{(Eq. A18)}$$

where $q_0 = cos(\frac{1}{2}\theta)$, $q_1 = sin\left(\frac{1}{2}\theta\right)u_X$, $q_2 = sin\left(\frac{1}{2}\theta\right)u_Y$ and $q_3 = sin\left(\frac{1}{2}\theta\right)u_Z$.

So, the position of the new Cartesian axes (*x*-*y*-*z*) after rotation with respect to the old coordinate system can be obtained by:

$$\begin{cases} \boldsymbol{Ox} = \boldsymbol{qOXq^{-1}} \\ \boldsymbol{Oy} = \boldsymbol{qOYq^{-1}} \\ \boldsymbol{Oz} = \boldsymbol{qOZq^{-1}} \end{cases} \quad \text{(Eq. A19)}$$

which yields:

$$\begin{bmatrix} \boldsymbol{Ox} \\ \boldsymbol{Oy} \\ \boldsymbol{Oz} \end{bmatrix} = T \begin{bmatrix} \boldsymbol{OX} \\ \boldsymbol{OY} \\ \boldsymbol{OZ} \end{bmatrix} \quad \text{(Eq. A20)}$$

where,

$$T = \begin{bmatrix} q_0^2 + q_1^2 - q_2^2 - q_3^2 & 2(q_1q_2 - q_0q_3) & 2(q_1q_3 + q_0q_2) \\ 2(q_1q_2 + q_0q_3) & q_0^2 - q_1^2 + q_2^2 - q_3^2 & 2(q_2q_3 - q_0q_1) \\ 2(q_1q_3 - q_0q_2) & 2(q_2q_3 + q_0q_1) & q_0^2 - q_1^2 - q_2^2 + q_3^2 \end{bmatrix} \quad \text{(Eq. A21)}$$

and $T^{-1} = T^T$. In fact, *T* is the rotation matrix in terms of quaternions. For multiple rotations, the rotation matrix can be determined by substituting $\boldsymbol{q}$ by the equivalent quaternion $\boldsymbol{q'}$.

- Application in the rotational resistance model

Since only spherical particles are considered, the directions of the body-frame coordinate system with the origin locating in the particle centroid always coincide with that of the space-frame (global) system. Taking the $\overrightarrow{Oz}$ axis in Figure F (b) as the contact normal and $\overrightarrow{OZ}$ as the

global *z* axis direction, the unit vector of the contact normal at the current time step can be expressed by:

$$\overrightarrow{Oz} = n_X \boldsymbol{i} + n_Y \boldsymbol{j} + n_Z \boldsymbol{k} \quad \text{(Eq. A22)}$$

in which $n_X = \frac{X_2 - X_1}{\sqrt{(X_2-X_1)^2+(Y_2-Y_1)^2+(Z_2-Z_1)^2}}, n_Y = \frac{Y_2 - Y_1}{\sqrt{(X_2-X_1)^2+(Y_2-Y_1)^2+(Z_2-Z_1)^2}}$ and $n_Z = \frac{Z_2 - Z_1}{\sqrt{(X_2-X_1)^2+(Y_2-Y_1)^2+(Z_2-Z_1)^2}}$ and $(X_1,Y_1,Z_1)$ and $(X_2,Y_2,Z_2)$ are the coordinates of the two touching particles in the global coordinate system.

Therefore, the vector that is orthogonal to both $\overrightarrow{OZ}$ and $\overrightarrow{Oz}$ can be determined by:

$$\boldsymbol{c} = \overrightarrow{OZ} \times \overrightarrow{Oz} = -n_Y \boldsymbol{i} + n_X \boldsymbol{j} \quad \text{(Eq. A23)}$$

and the rotation angle from $\overrightarrow{OZ}$ to $\overrightarrow{Oz}$ around $\boldsymbol{c}$ can be calculated by:

$$cos\theta = \frac{Z_2 - Z_1}{\sqrt{(X_2-X_1)^2+(Y_2-Y_1)^2+(Z_2-Z_1)^2}} \quad \text{(Eq. A24)}$$

Therefore the unit quaternion accounting for this rotation becomes,

$$q = \cos\left(\frac{1}{2}\theta\right) + \left(-\frac{n_Y}{\sqrt{n_X^2+n_Y^2}}\boldsymbol{i} + \frac{n_X}{\sqrt{n_X^2+n_Y^2}}\boldsymbol{j}\right)\sin(\frac{1}{2}\theta) \quad \text{(Eq. A25)}$$

This gives,

$$\begin{cases} q_0 = cos(\frac{1}{2}\theta) \\ q_1 = -sin\left(\frac{1}{2}\theta\right)\frac{n_Y}{\sqrt{n_X^2+n_Y^2}} \\ q_2 = sin\left(\frac{1}{2}\theta\right)\frac{n_X}{\sqrt{n_X^2+n_Y^2}} \\ q_3 = 0 \end{cases} \quad \text{(Eq. A26)}$$

Substituting Eq. A26 into Eq. A21, the rotation matrix T is obtained. Note that due to orthogonality, the X and Y axes after rotation, $\overrightarrow{Ox}$ and $\overrightarrow{Oy}$**,** are located in the contact plane. The transformation from global rotation to rotation around local axes from the previous time step to the current time step can thus be obtained by:

$$\begin{bmatrix} d\theta_x \\ d\theta_y \\ d\theta_z \end{bmatrix}_{t-\Delta t \to t} = T \begin{bmatrix} d\theta_X \\ d\theta_Y \\ d\theta_Z \end{bmatrix}_{t-\Delta t \to t} \quad \text{(Eq. A27)}$$

where $d\theta_x$ and $d\theta_y$ account for the relative rotation around the two orthogonal axes ($\overrightarrow{Ox}$ and $\overrightarrow{Oy}$) in the contact plane and $d\theta_z$ reflects twisting around the contact normal, $\overrightarrow{Oz}$. The inverse procedure is applied to perform the transformation from the local $dM_i$ to the global $dM_I$:

$$\begin{bmatrix} dM_X \\ dM_Y \\ dM_Z \end{bmatrix}_{t-\Delta t \to t} = T^{-1} \begin{bmatrix} dM_x \\ dM_y \\ dM_z \end{bmatrix}_{t-\Delta t \to t} \quad \text{(Eq. A28)}$$

The obtained global $dM_I$ are cumulatively added into the governing equation of angular motion. Considering that the real particle surface is rough rather than smooth, the contact radius $B$ is multiplied by a roughness index $\delta$ to give a corrected contact area, i.e., $\bar{k}_n = k_n/[\pi(\delta B)^2], \bar{k}_s = k_s/[\pi(\delta B)^2]$, $I = \frac{\pi}{4}(\delta B)^4$ and $J_z = \frac{\pi}{2}(\delta B)^4$. It is reasonable to restrict the corrected width to be smaller than the particle radius. Under this circumstance, $\delta$ should be in a range of 1 to 10 assuming a maximum 5% allowable overlap.

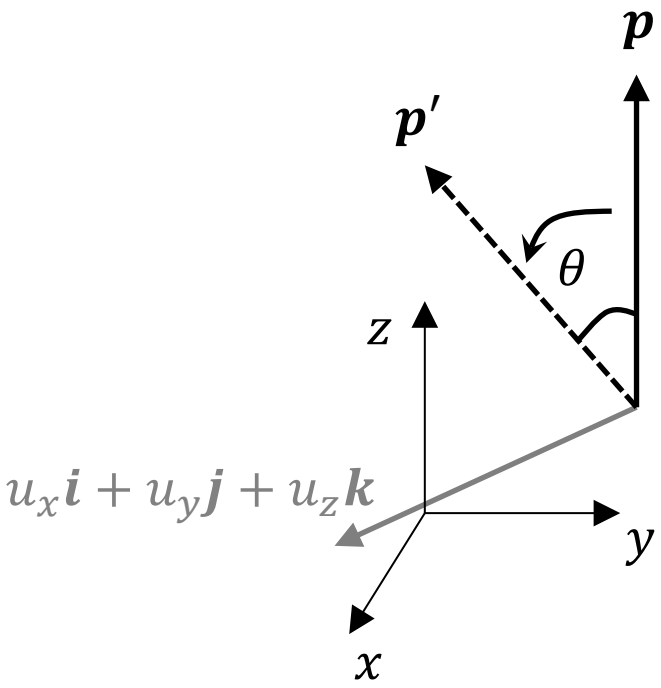


(a)

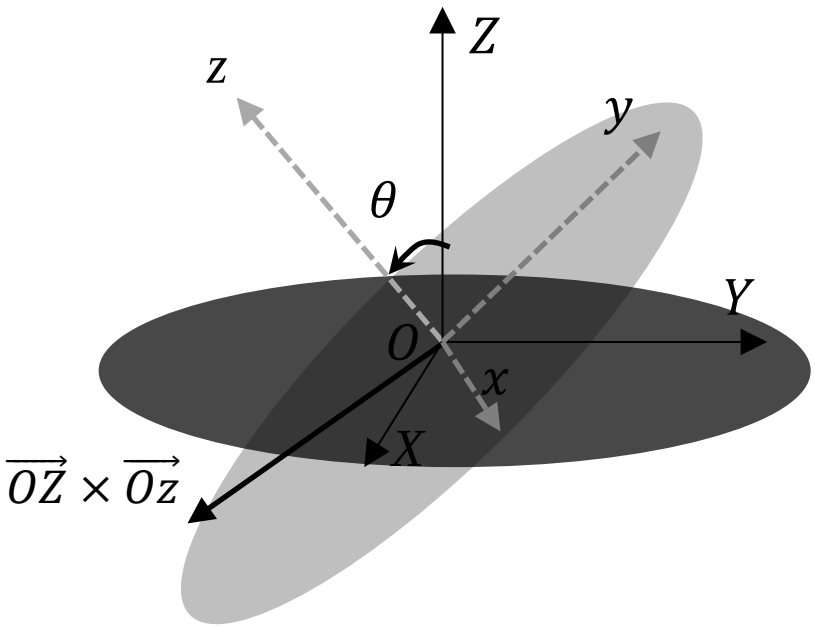


(b)

Figure F Applying quaternions to perform spatial rotation: (a) Rotation of a single vector around an arbitrary axis; (b) Rotation of a coordinate system around an axis that is orthogonal to the z axes of the old and new coordinate system

Considering that the real particle surface is rough rather than perfectly smooth, the contact radius $B$ is multiplied by a shape index $\delta$ to give a corrected contact area, i.e., $\bar{k}_n = k_n/[\pi(\delta B)^2], \bar{k}_s = k_s/[\pi(\delta B)^2]$, $I = \frac{\pi}{4}(\delta B)^4$ and $J_z = \frac{\pi}{2}(\delta B)^4$. It is reasonable to restrict the corrected width to be smaller than the particle radius. Under this circumstance, $\delta$ should be in a range of 1 to 10 assuming a maximum 5% allowable overlap.

**Limiting values for rotational resistance**

In reality, the asperities are not rigid, thus the rotational resistance cannot increase infinitely. A limiting value $M_r^m = \kappa f_n R_r$ ($R_r = \frac{r_1 r_2}{r_1 + r_2}$ is the rolling radius) is assigned to the rolling-induced contact moment $M_r$ in which $\kappa$ is a strength index which relates the strength of asperities to the normal contact force. Recognising that the magnitude of tangential shear flow $\tau$ is limited to $\mu \bar{f}_n$, where $\bar{f}_n$ is the normal contact force at the corresponding point, it is reasonable to assume the limiting value for the torque resistance to be the product of $\mu$ and $M_r^m$, i.e., $M_t \leq \mu\kappa f_n R_r$. The formulation for the resulting rotational resistance model is summarised in Eq. A29.

$$\begin{cases} M_{r,i} = \overline{k_n} I_i \theta_{r,i} \,\&\, M_{r,i} \le \kappa f_n R_r \ \ (i = x, y) \\ M_{t,i} = \overline{k_s} J \theta_{t,i} \,\&\, M_{t,i} \le \mu\kappa f_n R_r \ \ (i = z) \end{cases} \qquad \text{(Eq. A29)}$$